Sedimentologika

10.57035/journals/sdk.2026.e41.2307

Settling velocity of sediment grains, Part 2: Volume/area ratio as descriptor of particle size and shape in sediment hydrodynamics

Arnoud Slootman* [1,2], **Max de Kruijf** [3], **Guenther Glatz** [4], **Joris T. Eggenhuisen** [5], **Zane R. Jobe** [1], and **John J. G. Reijmer** [6]

[1]Department of Geology and Geological Engineering, Colorado School of Mines, Golden, CO, USA
[2]Division of Earth and Planetary Sciences, Graduate School of Science, Kyoto University, Kyoto, Japan
[3]TNO – Geological Survey of the Netherlands, Utrecht, The Netherlands
[4]Chemical & Petroleum Engineering, The University of Kansas, Lawrence, KS, USA
[5]Department of Earth Sciences, Utrecht University, Utrecht, The Netherlands
[6]Department of Earth Sciences, Faculty of Science, Vrije Universiteit Amsterdam, Amsterdam, The Netherlands

CRediT statement: *Writing-original draft*: AS, MdK. *Writing-review & editing*: JTE, JJGR, ZRJ. *Visualization*: AS, GG. *Conceptualization*: AS, MdK, JJGR. *Data curation*: AS, MdK, GG, JJGR. *Formal analysis*: AS, MdK, GG. *Investigation*: AS, MdK, GG, JJGR. *Methodology*: AS, MdK. *Software*: AS, GG. *Resources*: AS, JTE, JJGR. *Validation*: AS, MdK, GG. *Supervision*: JJGR. *Funding acquisition*: JJGR, ZRJ.

*Corresponding author: Arnoud Slootman, arnoudslootman@gmail.com

Abstract

Particle settling velocity is a fundamental property for sediment hydrodynamics with implications for sedimentology and engineering. Settling velocity depends on fluid properties and the density and dimensions of sediment grains. However, it is not self-evident what length variable should be chosen to represent particle size and shape in settling velocity equations. A companion paper (*Part 1*, Slootman et al., 2026) demonstrated that the ellipsoidal model as defined by the nominal diameter and a shape factor are unsuitable for the description of natural sediment particle dimensions. Mathematical derivation from the balance of forces between particle weight and fluid friction reveals that terminal settling velocity should be a function of particle volume and its maximum projection area. In this paper (*Part 2*) several candidates for a parameter representing particle dimensions in the settling problem are tested, including the diameters of the nominal and equivalent spheres, and the volume/area ratios of the bounding-box ellipsoidal model and the realistic particle model. The latter is obtained from high-resolution micro-computed tomography for 203 irregular skeletal carbonate grains, providing accurate ratios of particle volume over maximum projection area. This ratio predicts settling velocity more accurately than the other tested variables of particle size. Thus, the volume/area ratio captures both particle size *and* shape, which are usually modelled separately. This study proposes a new framework for accurate hydrodynamic characterisation of sediment particles.

Research Article

Executive Editor
Murray Gingras

Associate Editor
Siddhi Joshi

Reviewers
Pierre Weill
Siddhi Joshi

Production Manager
Jarred Lloyd

Copy Editor
Sophie Hage

Received: 2025-07-26
Accepted: 2026-01-14
Published: 2026-03-26

Keywords
settling velocity
grain size
particle shape
Reynolds number
drag coefficient

Plain language summary

Sediment particles accelerate when released in water due to the pull of gravity exceeding the friction between the particle and the fluid. As the particle picks up speed, the force due to fluid resistance increases until it balances with the weight of the particle. At this moment, the particle has reached terminal settling velocity. Because this parameter reveals insights into the friction between particles and water, settling velocity is an important variable in the hydrodynamic modelling of natural sediments. Prediction of particle settling velocity depends on the accurate description of particle size and shape, several candidates of which are tested in this paper. Our results demonstrate that the ratio of particle volume over its maximum projection area best captures the size and shape of sediment grains for the prediction of settling velocity.

1 Introduction

Sediment transport dynamics is key to understanding the distribution of sediments on Earth's surface (Hayes et al., 2021; Li et al., 2020) and potential preservation in the geological record (Anders et al., 1987; Brown et al., 2009). Aqueous flows are responsible for significant transfer of sediment particles along natural depositional environments (C. Wang et al., 2015), human-designed habitats (Fennessey & Jarrett, 1994; Yim, 1994) and infrastructures (Kondolf et al., 2014; Schleiss et al., 2016). Knowledge on the mechanisms of sediment erosion, transport, and deposition are therefore essential to numerous aspects of society (Parrinello & Kondolf, 2021). A fundamental parameter in sediment transport modelling is settling velocity (Dey et al., 2019; Le Roux, 2005), providing insights into the hydrodynamic properties of sediments such as transport modes (Camenen et al., 2006; Collins & Rigler, 1982; Dey & Ali, 2019) and the thresholds of sediment erosion (see Egiazaroff, 1965; and Hjulström, 1935; in Miedema, 2010), although their dependency on settling velocity is obscured for sediments comprising irregular particle shapes (e.g., Bian et al., 2023; Paphitis et al., 2002; Prager et al., 1996; Rieux et al., 2019; Smith & Cheung, 2004; Weill et al., 2010).

Terminal settling velocity represents the balance between the force of gravity acting on the sediment particle, and friction between the particle and the fluid (Clift & Gauvin, 1971; Stokes, 1850; Wadell, 1934). In terms of length parameters, gravity force depends on particle volume, and friction is controlled by maximum projection area. When this balance is solved for settling velocity, volume and area appear as a ratio (e.g., Riazi & Türker, 2019). Typically, the ratio of volume (L^3) over area (L^2) is reduced to a single length parameter (L). This simplification has led to the common assumption that settling velocity is a function of grain size alone, thereby overlooking the size *and* shape information captured by the volume/area ratio. As a consequence, attempting to find empirical relationships between settling velocity and grain size requires the introduction of shape descriptors (Dietrich, 1982; Slootman et al., 2026), such as the Corey (1949) shape factor, Powers (1953) roundness (Williams, 1966), sediment-specific constants (e.g., Ferguson & Church, 2004), or modification of a shape descriptor (e.g., Göğüş et al., 2001), all of which complicate predictive settling velocity models, in particular for irregular particles such as skeletal carbonates and volcaniclastics (see review in De Kruijf et al., 2021). A companion paper (*Part 1,* Slootman et al., 2026) evaluated the suitability of the nominal diameter and Corey shape factor, concluding that these parameters do not sufficiently describe particle size and shape of sediment grains in settling velocity models.

This study (*Part 2*) investigates the performance of fundamental settling velocity equations based on a simple linear relationship between dimensionless friction and dimensionless grain size, which are calculated using several length parameters. These length parameters are derived from the volume/area ratios obtained from the most common sediment particle models, including the bounding-box ellipsoid (Krumbein, 1941), equivalent sphere (Gibbs et al., 1971), and nominal sphere (Flemming, 1965). Their performance is contrasted with the volume/area ratio of a realistic particle model, generated with high-resolution micro-computed tomography (i.e., micro-CT). The different methods are tested on a sediment population composed of highly irregular skeletal carbonate grains. For sand-sized sediment grains, we show that volume/area ratio obtained from the realistic micro-CT particle model predicts settling velocity much better than any of the length parameters of the other models. The implications of these findings might be that micro-CT characterisation of (complex)

sediment grains is a necessary step in constraining the hydrodynamic properties of natural sediment.

2 Building a settling velocity model

2.1 Dimensional analysis

In the settling problem (Middleton & Southard, 1984), the two forces working on the particle and fluid are the submerged particle weight (i.e., the force of gravity minus the buoyant force) and the drag force caused by friction between the particle and the fluid (Figure 1). Submerged particle weight is straightforward to derive from the particle's volume and its density contrast with the fluid. The drag force, on the other hand, increases as the particle accelerates when falling through the fluid, until a balance of forces is attained and the particle has reached terminal settling velocity. The dependent variables of the drag force are the terminal settling velocity of the particle w_t, a length parameter L related to the dimensions of the particle, and the fluid's dynamic viscosity μ and density ρ_f (Table 1). Because the drag force is a function of settling velocity, once the balance of forces is achieved the equation can be solved for terminal settling velocity. To reduce the number of experiments required to derive an equation for settling velocity, the drag force and the combined dependent variables are made dimensionless. Then, only the variation between these two dimensionless parameters must be tested, rather than the effect of each dependent variable on the drag force separately. In addition, a dimensionless equation accounts for scaling effects, ensuring that the forces and motions in a scale model are physically similar to the real-world system (e.g., Paola et al., 2009).

2.2 Drag coefficient

The first step towards finding an equation for terminal settling velocity is to make the drag force F_D dimensionless by dividing it by a combination of dependent variables that together have the unit of force (Table 1). The dimensionless drag force is called the drag coefficient:

$$C_D = f\left(\frac{F_D}{L^2 \rho_f {w_t}^2}\right) \tag{1}$$

Equation 1 is not aimed at returning the magnitude of the drag force as a function of its dependent variables, but only serves to non-dimensionalise the drag force (Middleton & Southard, 1984). Hence, not all dependent variables need to appear in Equation 1 (e.g., dynamic fluid viscosity is not included). By convention, the drag coefficient in Equation 1 is written as:

$$C_D = \frac{F_D}{\frac{A}{2} \rho_f {w_t}^2} \tag{2}$$

where A is a characteristic area representing the particle. The typically used area is the maximum projection area as particles commonly fall perpendicular to this surface (Clift et al., 1978; Stringham et al., 1969). Also, Equation 2 only cancels the dimensions of the drag force, the value of which is still undetermined. The equation that returns the magnitude of the drag coefficient (and thus indirectly the magnitude of the drag force) should be a function of all dependent variables:

$$C_D = f\left(w_t, L, \mu, \rho_f\right) \tag{3}$$

2.3 Particle Reynolds number

The second step in constructing a settling velocity model is to find the relationship between the drag coefficient and the dependent variables (Equation 3). Because a dimensionless relationship is sought, the dependent variables are combined into another dimensionless variable (Table 1):

$$Re_p = \frac{\rho_f w_t L}{\mu} \tag{4}$$

Parameters of this form are referred to as Reynolds numbers (Reynolds, 1883). Reynolds numbers are a family of dimensionless numbers that are useful in describing the physical behaviour of systems dealing with fluid flow (Rott, 1990). More specifically, Reynolds numbers predict flow patterns (Figure 2; Fornberg, 1988; Peregrine, 1985), by indicating the momentum exchange per volume of the fluid in motion. On the one hand, fluid resists deformation due to molecular attraction between fluid particles in the form of viscous forces, represented by kinematic fluid viscosity (μ/ρ_f). On the other hand, the flowing fluid resists changes in velocity by exerting inertial forces, which depend on a velocity and a length scale. In laminar flow, in which fluid particles move in parallel flow lines, viscous forces are dominant. In turbulent flow, fluid particles move randomly causing chaotic changes in pressure and velocity, and hence inertial forces are dominant. Reynolds numbers thus predict flow patterns by computing the ratio between inertial forces and viscous forces (Figure 2).

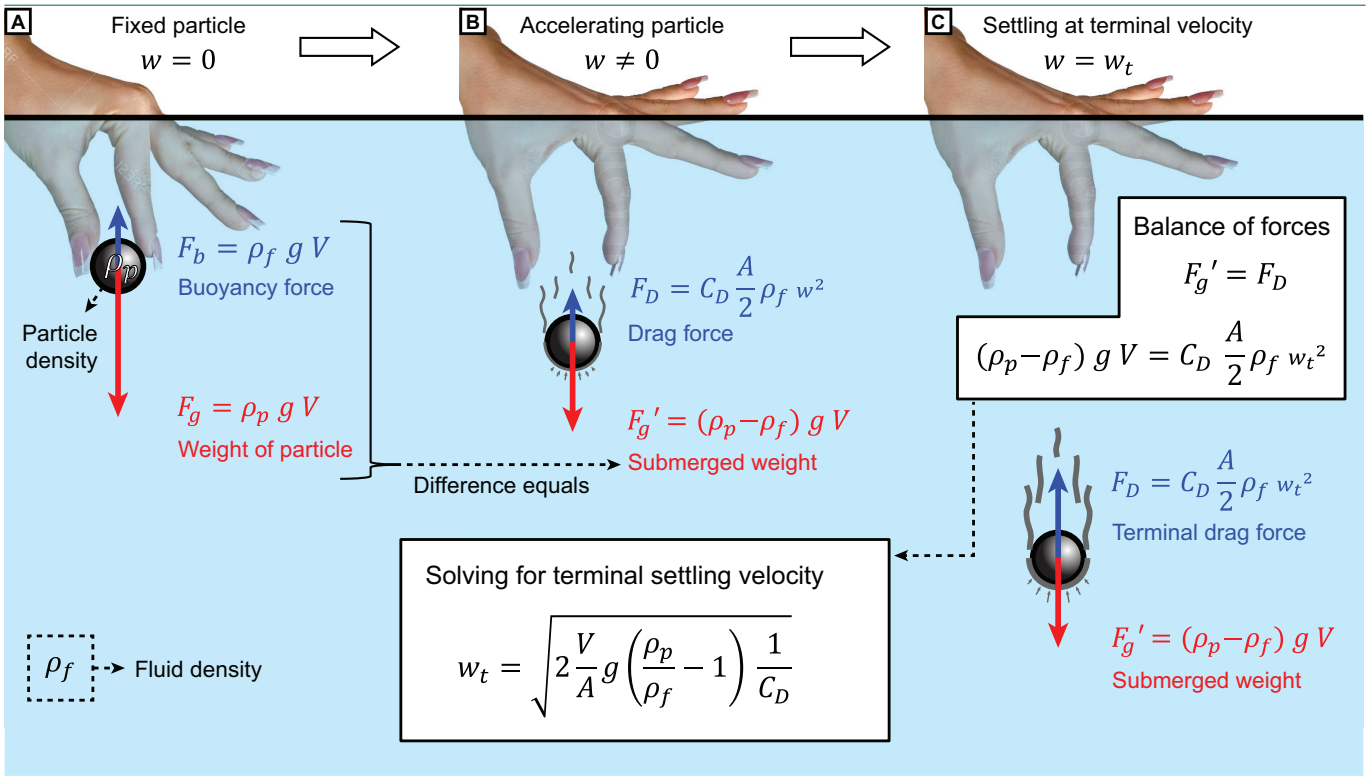

Figure 1 – **(A)** For a particle held under water, the weight is the downward force of gravity, and the upward buoyancy force equals the weight of the displaced water. **(B)** Submerged weight is the difference between weight and buoyancy force. Upon release, the movement of the particle through the fluid causes a resisting force (skin friction and form drag). For as long as the submerged weight exceeds this drag force, the particle accelerates. **(C)** Once a balance of forces is achieved (i.e., terminal drag force equals submerged weight), the particle falls with terminal settling velocity. For symbols see Appendix A and text.

Table 1 – Dimensional analysis of the settling problem.

Variable	Symbol/Equation	Dimensions in exponents			Units
		Mass (kg)	*Length (m)*	*Time (s)*	
Drag force	F_D	1	1	−2	$N = kg \cdot m \cdot s^{-2}$
Terminal settling velocity	w_t	0	1	−1	$m \cdot s^{-1}$
Length parameter	L	0	1	0	m
Dynamic viscosity	μ	1	−1	−1	$kg \cdot m^{-1} \cdot s^{-1}$
Fluid density	ρ_f	1	−3	0	$kg \cdot m^{-3}$
Drag coefficient	$C_D = \frac{F_D}{\rho_f \cdot w_t^2 \cdot L^2}$	0	0	0	$\frac{kg \cdot m^{-1} \cdot s^{-1}}{(kg \cdot m^{-3}) \cdot (m \cdot s^{-1})^2 \cdot m^2} = 1$
Particle Reynolds number	$Re_p = \frac{L \cdot w_t \cdot \rho_f}{\mu}$	0	0	0	$\frac{m \cdot (m \cdot s^{-1}) \cdot (kg \cdot m^{-3})}{kg \cdot m^{-1} \cdot s^{-1}} = 1$

There are two types of systems in which Reynolds number are useful: (1) systems in which the fluid moves through a confinement, and (2) systems in which fluid flows past an object (Middleton & Southard, 1984). In channel or pipe flows, the obvious length scale is the channel depth or the diameter of the pipe, and the velocity is that of the fluid flow. In the particle settling problem, the Reynolds number should represent the properties of the fluid and capture the dependency of flow patterns on a characteristic length scale and the settling velocity of the particle. This Reynolds number is called the particle Reynolds number, Re_p.

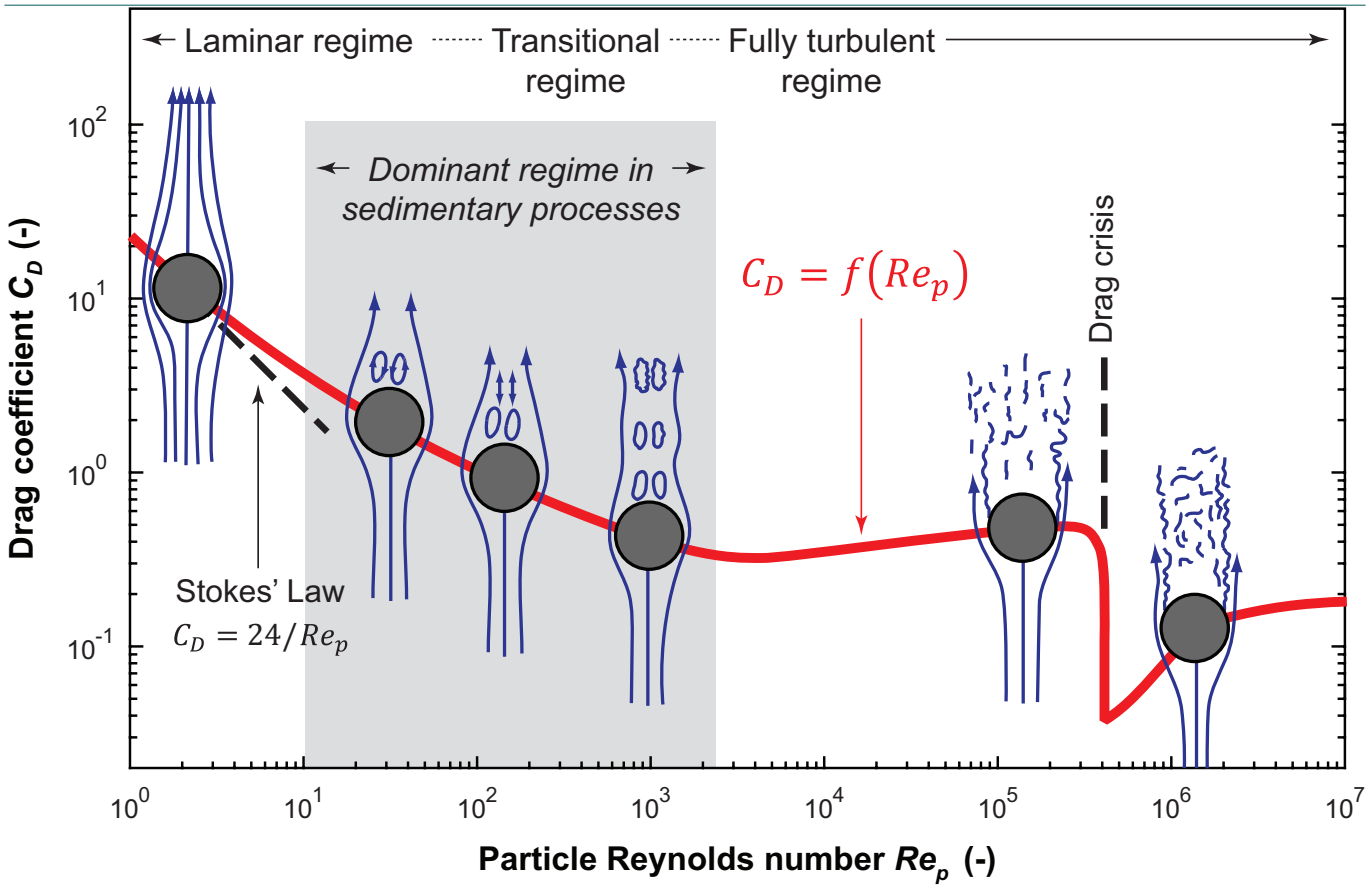

Figure 2 – Particle hydrodynamics as a function of two nondimensional parameters: (1) : particle Reynolds number, a dimensionless length scale obtained by the ratio of inertial forces to viscous forces, and (2) : drag coefficient, the ratio of drag force to dynamic pressure forces. Viscous forces dominate in laminar flow in the Stokesian realm. Inertial forces control turbulent flow in the Newtonian realm. The upper boundary of the laminar regime is placed at $Re_p = 10^{-}1$ (e.g., Bagheri & Bonadonna, 2016) to $Re_p = 10^0$ (e.g., Dey et al., 2019). Most sedimentary processes occur in the transitional regime up to $Re_p = 10^3$, proposed to be stretched to larger particle Reynolds numbers for irregular grain shapes (Smith & Cheung, 2003). The displayed $Re_p - C_p$ curve is from Fornberg (1988). Flow patterns in blue are modified from MIT OpenCourseWare in Southard (2006). Figure adapted from De Kruijf et al. (2021).

Settling velocity models essentially aim to solve the relationship between the drag coefficient and the particle Reynolds number:

$$C_D = f(Re_p) \tag{5}$$

Solutions to Equation 5 have the form of the red curve in Figure 2. For the viscous laminar regime (low particle Reynolds numbers), this equation was solved analytically by Stokes (1850). At larger particle Reynolds numbers (typical for sand grains from fine to medium sand size onwards; Southard, 2006), turbulent flow separation becomes important with the development of a wake behind the particle. Analytical solutions for turbulent flows only exist for conditions in which the flow is fully turbulent (DallaValle, 1948; Schlichting, 1975). However, most natural sedimentation processes take place in the transitional regime for which solutions to Equation 5 can only be solved empirically (e.g., Ahrens, 2003; Camenen, 2007; Cheng, 1997; Dietrich, 1982; Zhiyao et al., 2008). The relationship between the drag coefficient and the particle Reynolds number in the transitional regime is approximately linear at a double-logarithmic scale (Figure 2), as further employed later in this paper.

2.4 A length parameter for settling velocity

The terminal settling velocity of a sediment particle can thus be obtained from the balance of forces between submerged particle weight and terminal drag force (Figure 1). The constant magnitude of the submerged particle weight is given by:

$$F_g' = (\rho_p - \rho_f) g V \tag{6}$$

where g is gravitational acceleration, and ρ_p and ρ_f the densities of the particle and fluid. The dimensional form of the terminal drag force is found by rewriting Equation 2:

$$F_D = C_D \frac{A}{2} \rho_f w_t^2 \tag{7}$$

For as long as there is no balance of forces, the net difference between F_g' and F_D is the force that causes the particle to accelerate as predicted by Newton's second law of motion. Acceleration halts once the forces balance, and the particle falls at its terminal velocity, w_t. By equating submerged weight and terminal drag force (Table 2A), a general equation for terminal settling velocity is obtained:

$$w_t = \sqrt{2\frac{V}{A}g\left(\frac{\rho_p}{\rho_f} - 1\right)\frac{1}{C_D}} \tag{8}$$

It thus follows that the characteristic length scale L in the settling velocity problem is the particle's volume/area ratio. This finding shines new light on the particle Reynolds number in Equation 4, in which the length parameter should thus be replaced with V/A.

There are several models to approximate the spatial distribution (i.e., the size and shape) of sediment particles. If a high-definition scan is available, e.g., as obtained using micro-CT, the measured volume and area are very close to the actual dimensions of the particle (Figure 3A). Other measurement techniques (e.g., caliper measurement or image analysis) provide the dimensions of a bounding box that circumscribes the particle (Blott & Pye, 2008; Krumbein, 1941). The long, intermediate, and short axes of the bounding box are then used to construct an ellipsoid as a representation of the particle's size and shape (Figure 3B). The volume/area ratio of an ellipsoid is a function solely of its short diameter (Table 2B).

Alternatively, there are two popular spherical models: the equivalent and nominal spheres, which yield length parameters here called equivalent diameter and nominal diameter. Because these terms are not always used as originally intended they may cause confusion. Wadell (1934) introduced a nominal sphere that has the same volume as the actual particle. However, Flemming (1965) noted that the actual particle volume is difficult to obtain and suggested that the approximate ellipsoidal volume can be used instead to obtain the nominal diameter. The approximate nominal diameter of Flemming (1965) is often just called nominal diameter, which is the term adopted in this study. The spherical diameter of Wadell (1934) is referred to as the true nominal diameter, sometimes named the diameter of the volume-equivalent sphere (e.g., Y. Wang et al., 2018). Here, this length parameter is called equivalent diameter. Volume-equivalent spherical diameter is not to be confused with the equivalent sedimentation diameter of Gibbs et al. (1971), where it is used as the diameter of a sphere of quartz composition that attains the same settling velocity as the particle under investigation. Thus, the equivalent sphere has the same volume as the actual particle (Figure 3C; Wadell, 1934), and the nominal sphere has the volume of the bounding-box ellipsoid (Figure 3D; Flemming, 1965).

Spherical models do not capture particle shape, but only provide a measure of grain size. The visual overview in Figure 3 demonstrates that for irregular sediment grains there are large differences between models in representing the particle volume and maximum projection area. If the characteristic length parameter in the settling problem is V/A (Table 2B), then the choice of particle model will have significant implications for the performance of the settling velocity model.

3 Dataset

A dataset containing the terminal settling velocities of highly irregular, skeletal carbonate sediment particles was selected to test the performance of the different particle models in the settling velocity problem (Figure 4). These particles originate from a cool-water carbonate factory (*sensu* Reijmer, 2021; Schlager, 2003) and include the skeletal remains of red algae, bivalves, bryozoans, benthic foraminifers, echinoids, serpulids, and barnacles (Slootman et al., 2019). The dataset contains 203 particles of dominantly coarse and very coarse sand size, which were scanned at 10 µm resolution using a FEI Heliscan micro-CT (Thermo Fisher Scientific, Waltham, MA, USA) at the Center for Integrative Petroleum Research at King Fahd University in Dhahran, Saudi Arabia (see Slootman et al., 2023 for a detailed analytical description). The digital models thus obtained provide the volume (including intra-particle porosity) and maximum projection area of each particle. In addition, the 'maximum' bounding box (i.e., the box for which the longest particle axis and longest box axis are aligned; see Bagheri et al., 2015) was determined, providing the long, intermediate, and short axes of the bounding-box ellipsoid. Axial dimensions were used to calculate shape distribution through the Corey shape factor. A visual overview of the spread in shape is shown in the flatness-elongation diagram of Zingg (1935) (Figure 4B). Shape is widely distributed among

		Measured particle parameters		Computation	Length parameter representing volume/area
Realistic particle model	Voxel-model approximating the spatial dimensions of the particle (*e.g.*, micro-CT).	Particle volume	V_{meas}	———	Measured volume/area $\left(\frac{V}{A}\right)_{meas}$
		Particle maximum projection area	A_{meas}		
Bounding-box ellipsoid	Ellipsoid with the same axial dimensions as the bounding box.	Short diameter	D_s	———	Short diameter $\frac{2}{3} D_s$ = Calculated volume/area $\left(\frac{V}{A}\right)_{calc}$
Equivalent sphere	Sphere with the same volume as the particle.	Particle volume	V_{meas}	Equivalent diameter $D_{eq} = \sqrt[3]{\frac{6}{\pi} V_{meas}}$	Equivalent diameter $\frac{2}{3} D_{eq}$
Nominal sphere	Sphere with the same volume as the bounding-box ellipsoid.	Long diameter	D_l	Nominal diameter $D_n = \sqrt[3]{D_l D_i D_s}$	Nominal diameter $\frac{2}{3} D_n$
		Intermediate diameter	D_i		
		Short diameter	D_s		

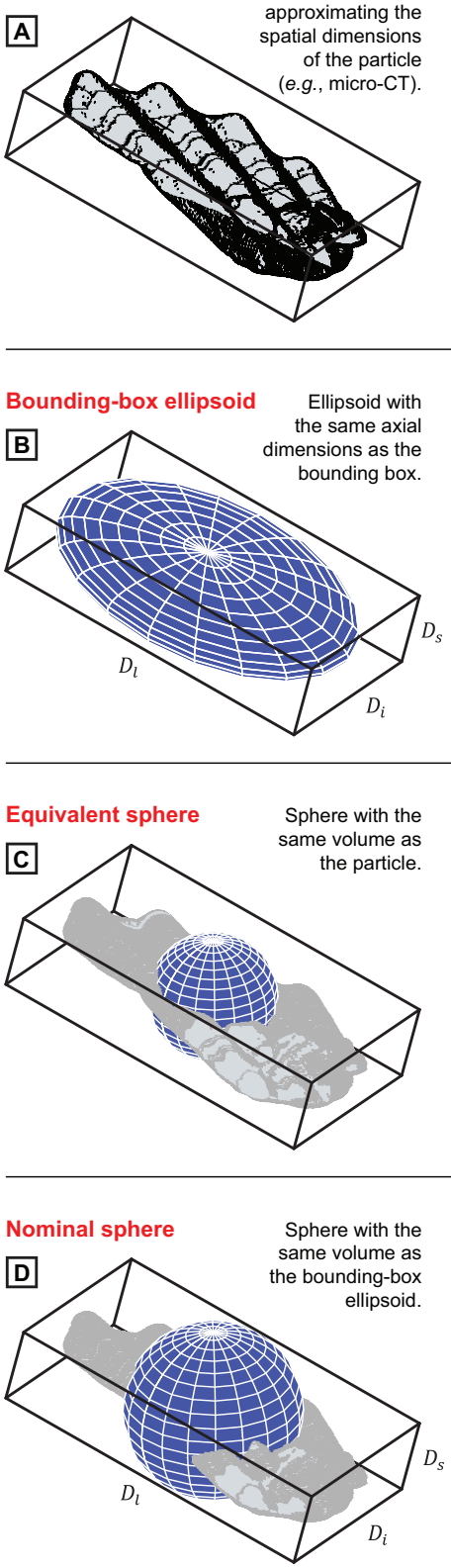

Figure 3 – Particle models. **(A)** Realistic particle models as acquired using micro-CT provide non-approximated volume and area yielding a more truthful V/A ratio. This is especially relevant for irregular sediment particles like skeletal carbonate grains such as the bivalve fragment shown here. **(B)** V/A ratio of an ellipsoid with the diameters of the bounding box is 2/3 of the short diameter. **(C)** V/A ratio of the equivalent-sphere model returns 2/3 of the equivalent diameter, i.e. the diameter of a sphere with a volume equal to the measured volume of the particle. **(D)** V/A ratio of the nominal-sphere model is 2/3 of the nominal diameter, calculated as the cubic root of the product of the bounding-box dimensions.

Table 2 – Characteristic length parameters in the settling velocity problem. See Appendix A for symbols.

[A]	General Equations
Submerged particle weight	$F'_G = g\left(\rho_p - \rho_f\right)V$
Terminal drag force	$F_D = C_D \frac{A}{2} \rho_f {w_t}^2$
Terminal settling velocity ($F'_G = F_D$)	$w_t = \sqrt{2\frac{V}{A}g\left(\frac{\rho_p}{\rho_f} - 1\right)\frac{1}{C_D}}$

[B]	General particles	Ellipsoidal particles	Spherical particles
Particle volume	V	$V = \frac{\pi}{6} D_l D_i D_s$	$V = \frac{\pi}{6} {D_n}^3$
Maximum projection area	A	$A = \frac{\pi}{4} D_l D_i$	$A = \frac{\pi}{4} {D_n}^2$
Volume/area ratio	$\frac{V}{A}$	$\frac{V}{A} = \frac{2}{3} D_s$	$\frac{V}{A} = \frac{2}{3} D_n$
Terminal settling velocity	$w_t = \sqrt{2\frac{V}{A}g\left(\frac{\rho_p}{\rho_f} - 1\right)\frac{1}{C_D}}$	$w_t = \sqrt{\frac{4}{3} D_s g\left(\frac{\rho_p}{\rho_f} - 1\right)\frac{1}{C_D}}$	$w_t = \sqrt{\frac{4}{3} D_n g\left(\frac{\rho_p}{\rho_f} - 1\right)\frac{1}{C_D}}$

the particles, which makes the dataset suitable for testing the influence of the choice of particle model on the performance of settling velocity equations. The mass of each individual particle was determined on an accurate balance with 0.01 mg precision, which was then used to determine particle density (i.e., the density of the solid mineral and water-filled porosity, see De Kruijf et al., 2021 for a discussion on carbonate particle densities). In addition to the dimensional properties and density, Slootman et al. (2023) measured the terminal settling velocity of each particle, as well as density and dynamic viscosity of the water in a 200 cm tall settling column. Hence, all dependent variables are available for each particle in the dataset (see supplementary materials).

4 Methods

4.1 A linear equation for $C_D = f\left(Re_p\right)$

Settling velocity models were constructed for the different length parameters representing volume/area ratio to evaluate the suitability of each of the particle models (Figure 3). For each particle, the measured dependent variables were used to calculate particle Reynolds number with Equation 4, and experimental drag coefficient by rewriting Equation 8 into:

$$C_{D,exp} = 2\,L\,g\left(\frac{\rho_p}{\rho_f} - 1\right)\frac{1}{{w_{t,exp}}^2} \tag{9}$$

where L is the tested length parameter (see Figure 3), and $w_{t,exp}$ is the terminal settling velocity as found in experiments. Particle Reynolds numbers in the dataset (n = 203) occur over the range $5 < Re_p < 360$, i.e., in the transitional regime between laminar and fully turbulent flow conditions (e.g., Dey et al., 2019). The relationship $C_D = f\left(Re_p\right)$ is approximately linear in this domain when plotted on double-logarithmic scale (Figure 2). Hence, linear regression can be applied to find the relationship between $\log_{10}\left(Re_p\right)$ and $\log_{10}\left(C_D\right)$. As a demonstration of the methodology, the $Re_p - C_{D,exp}$ data points for the measured V/A ratio as length parameter are plotted at both linear and logarithmic axes in Figure 5. At linear scale, the best-fitting curve through the data points is a power function of the form:

$$C_D = 10^b\, {Re_p}^a \tag{10}$$

At logarithmic scale, the best-fitting curve through the same data points is a linear function:

$$\log_{10}\left(C_D\right) = a\,\log_{10}\left(Re_p\right) + b \tag{11}$$

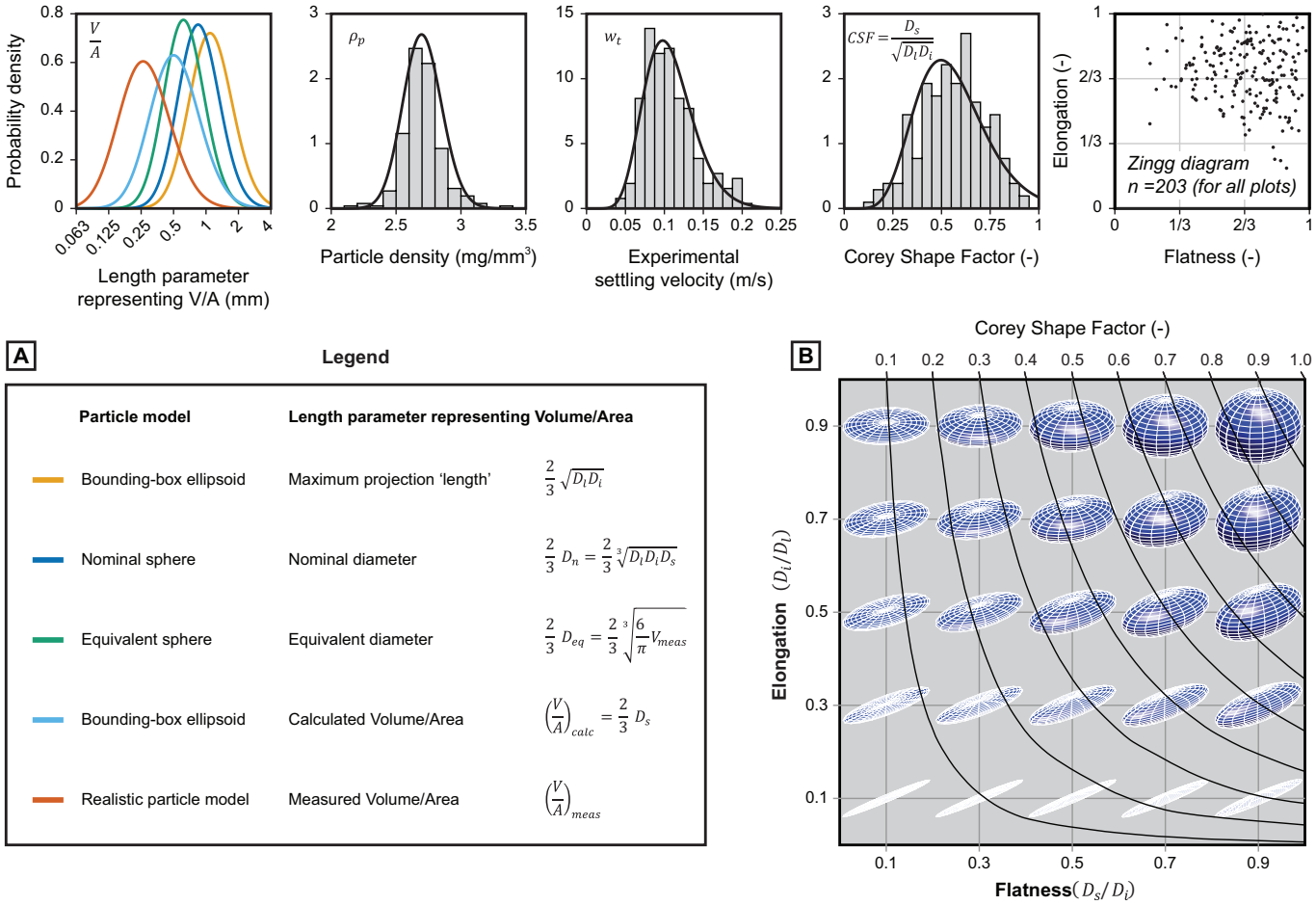

Figure 4 – Particle models. **(A)** Properties of 203 irregular skeletal carbonate sand particles in the dataset used in this study. Grain-size distribution varies greatly with the chosen particle model. Distribution of particle shape is expressed with Corey shape factor (*CSF*). Particle flatness versus elongation is plotted in the Zingg (1935) diagram. Probability density functions are normal-gamma distributions (Vaz & Fortes, 1988). Data from Slootman et al. (2023). **(B)** Distribution of ellipsoidity in the Zingg diagram with *CSF*-isolines. **(C)** See Slootman et al. (2023) for details on particle composition.

The scalars a and b in Equation 11 have the same values as those in Equation 10, because both equations represent the same relationship between the plotted combinations of drag coefficient and particle Reynolds number. Therefore, also the coefficients of determination (R^2) are identical for both fitted functions. Hence, linear regression can be applied to find the relationship $C_D = f(Re_p)$.

4.2 Iteration process

Each of the settling velocity models (i.e., one for every particle model) essentially consists of the fitted function $C_D = f(Re_p)$, as represented in Equation 10 and Figure 5. The purpose of a settling velocity model is that with the measured particle and fluid properties, a drag coefficient can be obtained that is then used to calculate the settling velocity of that particle as predicted by the model. However, the calculation of C_D is based on a particle Reynolds number, which is itself a function of settling velocity. The calculation of terminal settling velocity as predicted by the model, therefore, requires an iteration process (Figure 6). An estimated Re_p that falls within the range of experimental particle Reynolds numbers (e.g., Re_p = 100) is used to calculate a drag coefficient with the fitted function in Equation 10. This calculated drag coefficient is inserted into the general settling velocity equation (Equation 8), together with the fluid properties and particle length parameter and density. A more accurate Re_p is computed with the newly calculated settling velocity, which is then used to repeat the iteration. The absolute error between successive iterations of calculated settling velocity is determined (Figure 6). Once the error falls below the tolerance, here set at 1 %, the calculated terminal settling velocity for that specific particle has been found (typically within four to five iterations). The iteration process was performed for each particle individually.

4.3 Error analysis

Error analysis was used for the drag coefficient obtained using the fitted function (Equation 10, see also Figure 5) and terminal settling velocity using the iteration process. Relative error ε is determined through:

$$\varepsilon = \left(\frac{\text{calculated value}}{\text{measured value}} - 1 \right) 100\,\% \qquad (12)$$

for which positive and negative outcomes are possible. Error analysis involves the calculation of relative error for each particle separately, which enables evaluating the performance of each settling velocity model as an error distribution. Normal-gamma distributions (Vaz & Fortes, 1988) are used to obtain probability density functions of relative error distribution, because it allows for an asymmetrical probability distribution around the mean. The mean μ of the relative error distribution represents the accuracy of the model (i.e., the closeness of the calculated values to the experimental values). The standard deviation σ of the relative error distribution is a measure of the precision of the model (i.e., the spread in the difference between calculated and experimental values). Error analysis can also be captured with the mean absolute error (MAE):

$$MAE = \frac{1}{n} \sum abs(\varepsilon) \qquad (13)$$

which returns a single parameter indicating the degree of scatter of the data points from the 1:1 relationship, on which the calculated values exactly match the experimental values.

5 Settling velocity is a function of volume/area ratio

Terminal settling velocity is a function of the volume/area ratio of the sediment particle as shown in Equation 8. The chosen particle model determines the length parameter representing volume/area ratio (Figure 3). A realistic particle model as obtained from micro-CT provides the most accurate ratio: $(V/A)_{meas}$. Volume/area ratios from other models are not measured directly but are calculated (Figure 3). The only other model that is based on measured volume is the equivalent sphere. Spherical models return a diameter multiplied by a factor $\frac{2}{3}$ to represent volume/area ratio (Figure 3; Table 2B). Other models are based on an ellipsoid with the axial dimensions of the bounding box that circumscribes the particle, where the volume/area ratio of ellipsoids is a function of the short diameter of the ellipsoid multiplied by a factor $\frac{2}{3}$ (Figure 3B). Another length parameter that was tested is the 'maximum projection diameter' of the ellipsoid: $\frac{2}{3}\sqrt{D_I D_i}$.

The performance of these five length parameters was evaluated by building a settling velocity model for each of the length parameters using the dataset of irregular skeletal carbonate grains. Particle Reynolds numbers and experimental drag coefficients were

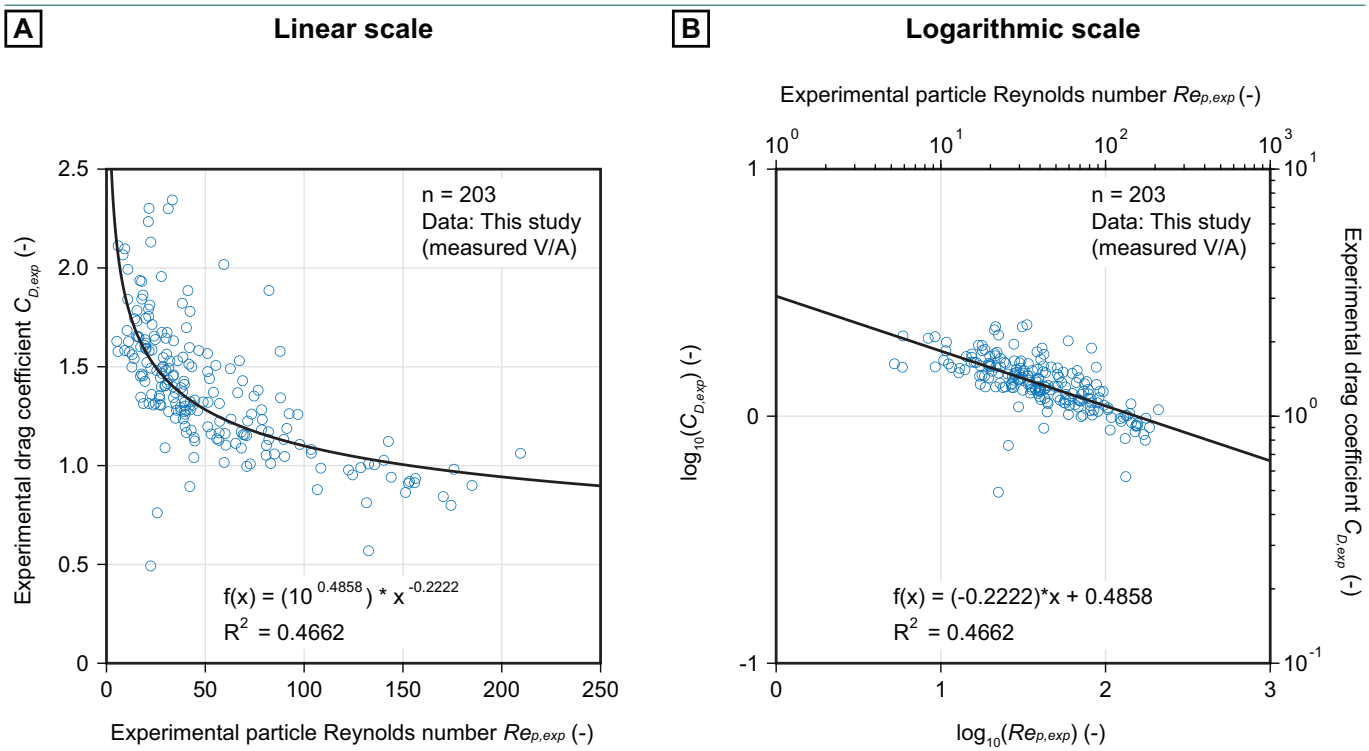

Figure 5 – **(A)** Logarithmic curve-fitting at linear scale. **(B)** Linear curve-fitting at logarithmic scale. Identical data have been used in both plots, hence the same R^2 is found for both functions, which are thus essentially the same.

obtained through Equations 4 and 9. Settling velocity models were constructed using linear regression (i.e., Equation 11 represented by functions $f(x)$ in Figure 7A), which were then used to calculate drag coefficients through Equation 10 (Figure 7B). Performance of the settling velocity models in predicting C_D was evaluated through the distribution of relative errors (Figure 7C). Using the iteration processes, calculated terminal settling velocities were obtained and compared against known experimental values (Figure 7D). Relative error distributions of calculated settling velocity were generated for each of the tested length parameters (Figure 7E).

The best-performing particle length parameter for the prediction of terminal settling velocity is the measured volume/area ratio as obtained from the realistic particle models created using micro-CT (Figure 7). Despite a low goodness of fit (R^2 = 0.4662) for the constructed $Re_p - C_D$ relationship for $(V/A)_{meas}$ (Figure 7A), the accuracy and precision of the relative errors and the mean absolute error of this length parameter ratio demonstrate much better ability to predict drag coefficients than any of the other particle models (Figure 7B, C). This outperformance is reflected in the predicted settling velocities using measured volume/area ratio, showing an excellent fit to measured values (R^2 = 0.8884) and lower errors (Figure 7D, E). All other particle models overpredict the mean settling velocity and generate much wider (i.e., less precise) distributions in predicted values. Thus, the best particle model for predicting settling velocity is the realistic particle model as obtained from micro-CT. Second best is the bounding-box ellipsoid particle model, followed by the equivalent spherical model, and then the nominal spherical model. The maximum projection diameter of the ellipsoid performs the poorest in representing a characteristic length parameter of sediment particles in the settling velocity model.

The ability of the realistic particle model in predicting terminal settling velocity of sediment particles is further analysed in Figure 8. Data points are colour-coded by Corey shape factor, which provides a measure of particle ellipsoidity through $CSF = D_s/\sqrt{D_l D_i}$ (see isolines in the Zingg diagram in Figure 4B). Density differences between particles did not contribute to the error between predicted and measured settling velocity, because the density of individual particles as determined by micro-CT was used as input in the predictions. Inspection of shape differences, however, reveals that for similar grain sizes, particles with higher sphericity reach higher settling velocities than flatter or more elongated particles (see Corey shape distribution in Figure 8; see also Slootman et al., 2023). Yet, the scatter of *CSF*-values across the 1:1 relationship indicates that ellipsoidity does not explain

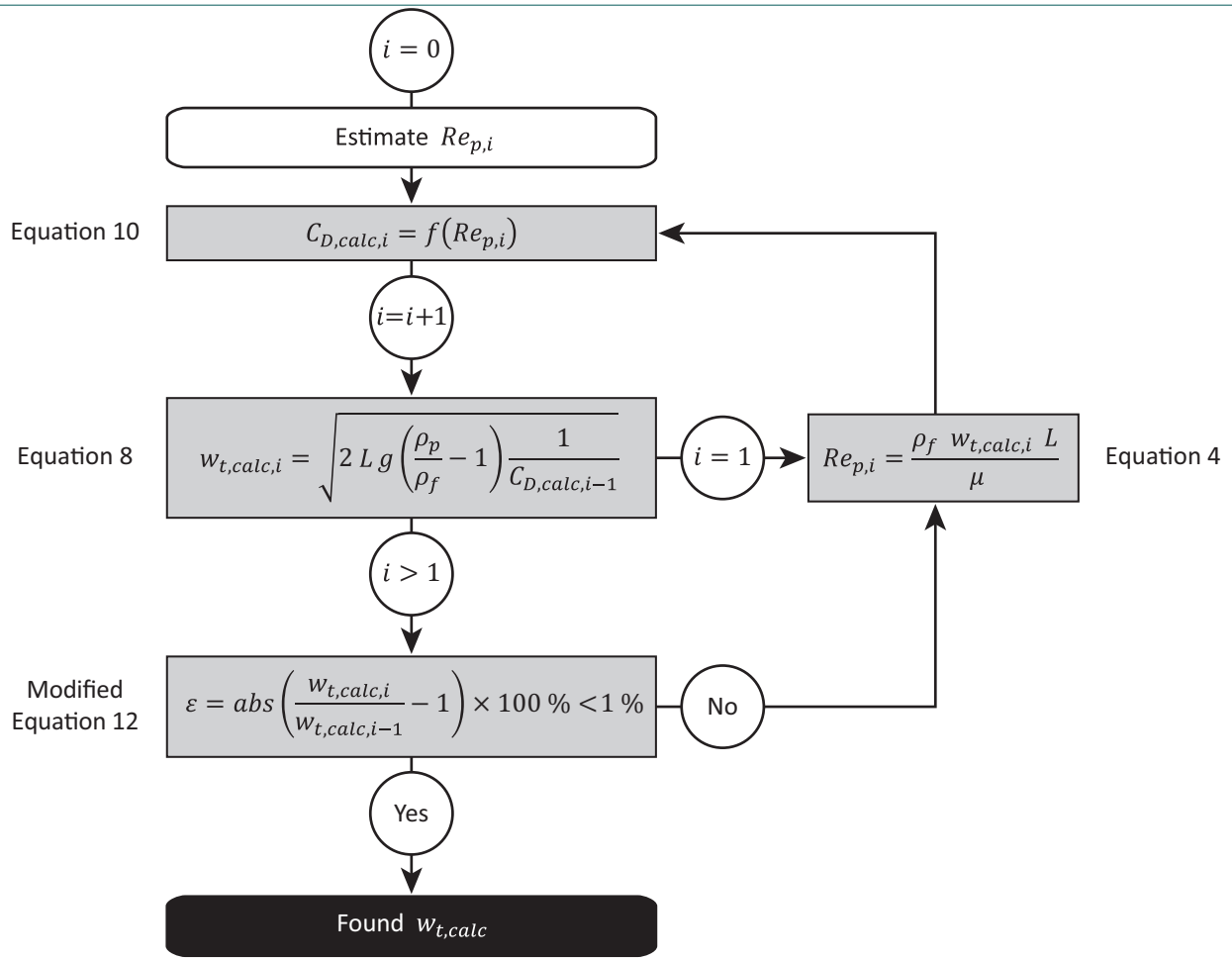

Figure 6 – Iteration process for the calculation of terminal settling velocity using particle and fluid properties. Using an estimated particle Reynolds number in the range of experimental values (e.g., Re_p = 100), a value for the terminal drag coefficient is calculated using the function found through curve-fitting (Equation 10, Figure 5). This $C_{D,calc}$ is then used as input variable, together with the experimentally determined particle and fluid properties, to calculate terminal settling velocity using the general equation (Equation 8). Variable *L* represents the particle length parameter as obtained from the chosen particle model (Figure 3). For the first iteration *i* = 1, $w_{t,calc}$ is used to obtain a more accurate Re_p with Equation 4, which is then used to recalculate a more accurate $C_{D,calc}$. For subsequent iterations, calculated terminal settling velocity is compared with the value obtained from the previous iteration by computing the absolute error (absolute value of relative error in Equation 12). If the absolute error exceeds the tolerance of 1 %, then the iteration is repeated. If the absolute error is acceptable, then the final calculated terminal settling velocity has been found for that specific particle. This iteration process is carried out for each particle individually.

the distribution in relative error between calculated and experimental settling velocity. Other factors that influence settling velocity of sediment particles include the angularity of particle corners and the roughness of the particle surface, in addition to asymmetry in particle shape (see review in De Kruijf et al., 2021). The volume/area ratios tested in this study, either obtained through direct measurement or by computing axial ratios of the bounding box, thus, do not account for all the factors that influence terminal settling velocity. However, as a first-order estimate, these variables provide an acceptable approximation of particle size and shape required to predict settling velocity, especially given that the dataset is composed of heterogeneous carbonate grains.

6 Comparison of settling velocity models

6.1 Settling velocity models for irregular carbonate particles

Several equations for the settling velocity of complex sediment particles of carbonate composition have been proposed previously; most notably Alcérreca et al. (2013), Y. Wang et al. (2018), and Riazi et al. (2020). These three studies use three different particle datasets documenting the principal axes of each particle (see Slootman et al., 2026 for a summary of these datasets).

Alcérreca et al. (2013) collected an original dataset of tropical carbonate sediment from the Gulf of

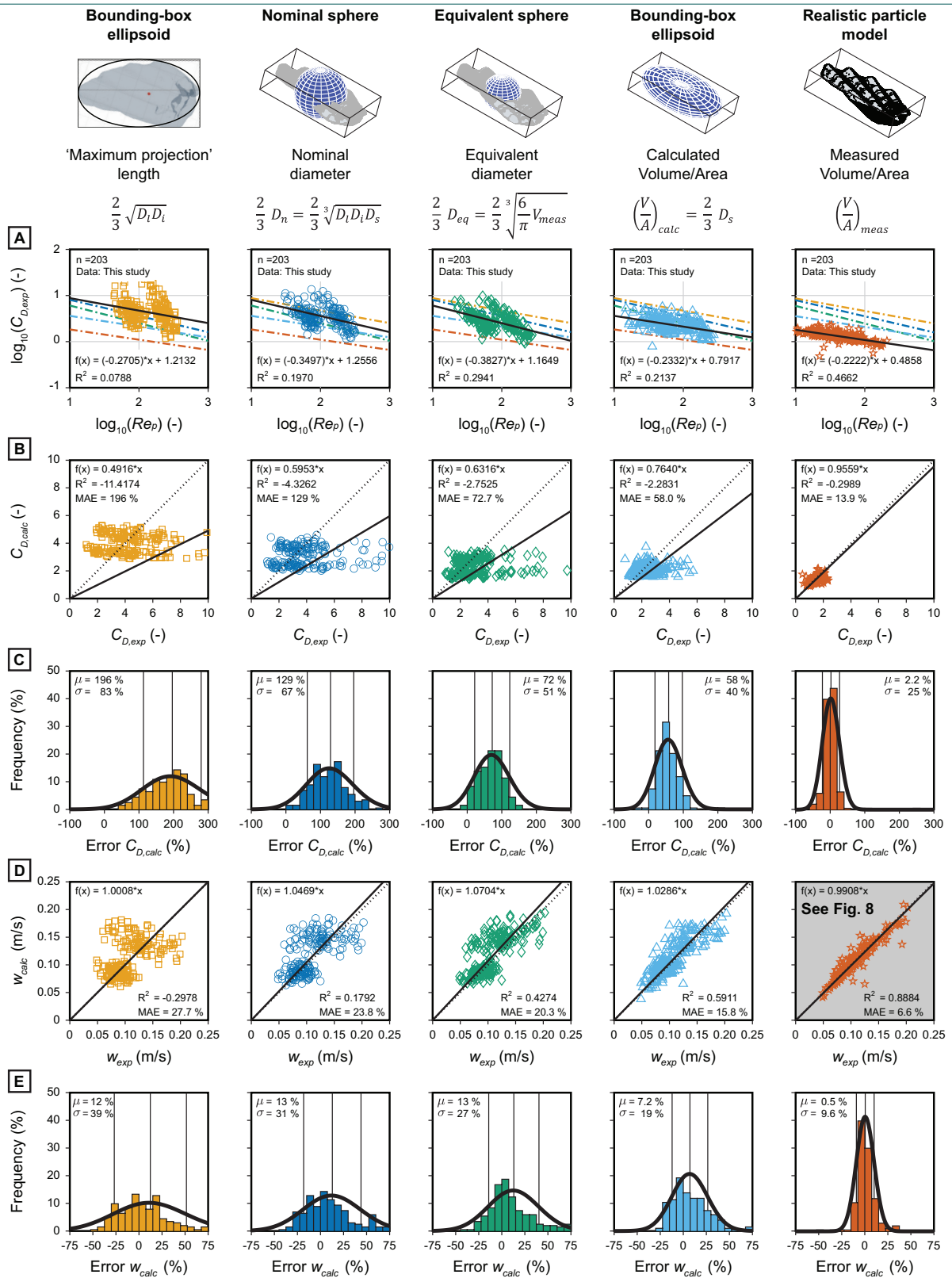

Figure 7 – Hydrodynamic parameters and error distributions for evaluated particle length parameters. **(A)** Particle Reynolds number (Equation 4) versus experimental drag coefficient (Equation 9). Solid black line is function $f(x)$ that represents the constructed settling velocity model in Equation 11. Dashed lines are the curves of the other models. **(B)** Experimental versus calculated drag coefficient. Solid line is $f(X)$ representing the function of linear regression forced through the origin. **(C)** Distribution of relative error for experimental versus calculated drag coefficient (Equation 12). **(D)** Experimental versus calculated terminal settling velocity. Solid line is $f(X)$ representing the function of linear regression forced through the origin. **(E)** Distribution of relative error for experimental versus calculated terminal settling velocity (Equation 12). Performance of settling velocity models increases towards the right in the figure. *MAE* is mean absolute error (Equation 13). Probability density functions are normal-gamma distributions (Vaz & Fortes, 1988) for which mean μ (model accuracy) and standard deviation σ (model precision) are shown. Dashed line is the 1:1 relationship on which the calculated values exactly match the experimental values.

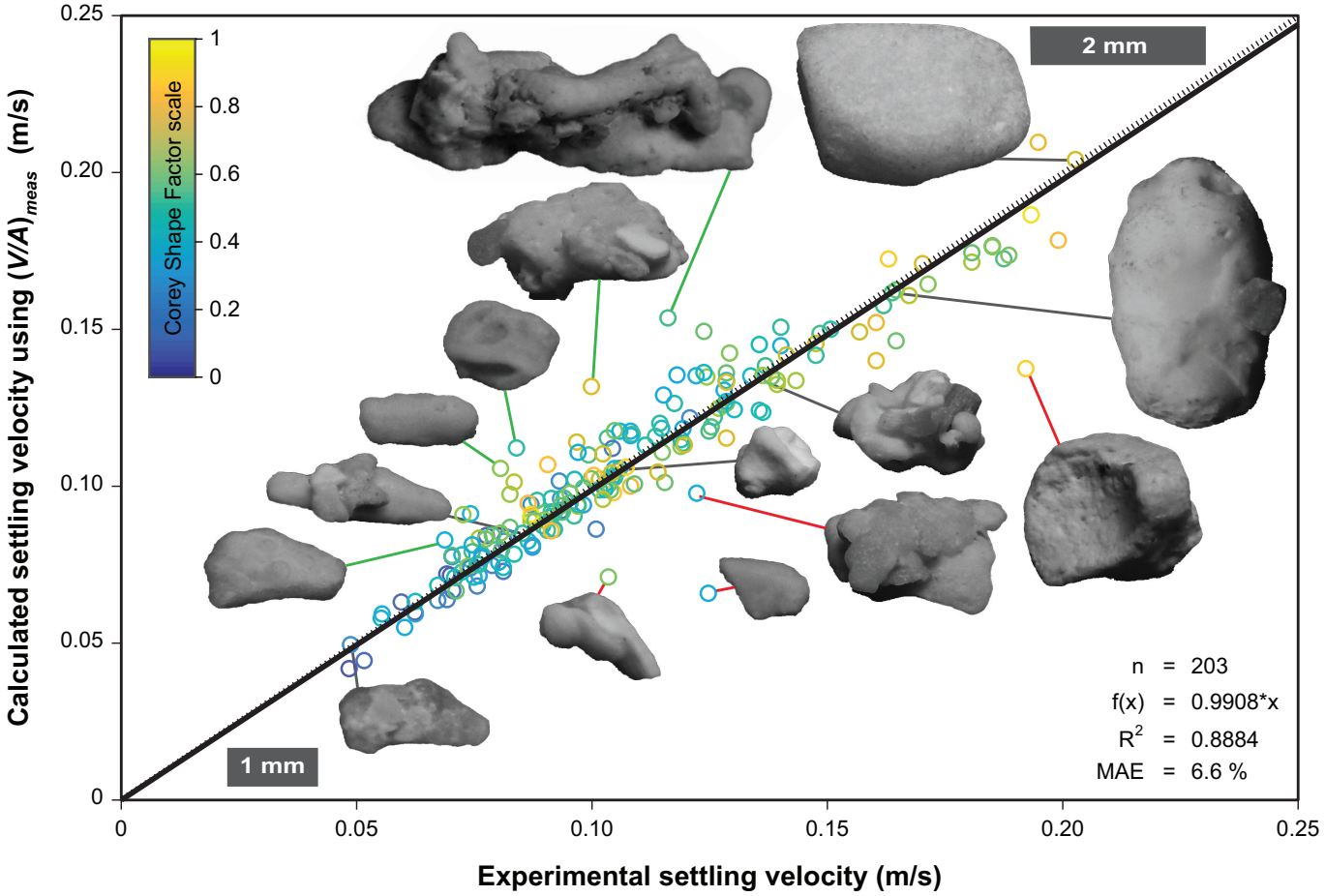

Figure 8 – Close-up of plot in Figure 7D, showing experimental versus calculated terminal settling velocity for measured volume/area ratio as obtained from micro-CT (realistic particle model). Data points are colour-coded by Corey shape factor as a measure of particle ellipsoidity ($CSF = D_s/\sqrt{D_I D_i}$, see also Figure 4B). Particle photos are shown for several data points. This plot demonstrates that particle ellipsoidity cannot explain all the dependency that particle shape has on settling velocity. Other factors influencing settling velocity include particle angularity and surface roughness, as well as asymmetry in particle shape, which are not accounted for by axial ratios as tested in this study. Solid line is $f(x)$ representing the function of linear regression forced through the origin. Dashed line is the 1:1 relationship on which the calculated values exactly match the experimental values. *MAE* is mean absolute error (Equation 13).

Mexico, using the long, intermediate, and short axes of 1 557 particles, obtained using a photographic technique involving shadows and trigonometry, to calculate nominal diameters in the range of 0.125 to 1 mm Based on measured settling velocity, nominal diameter, and density of each particle, Alcérreca et al. (2013) proposed:

$$Re_p = \left(\sqrt{22 + 1.13{D_*}^2} - 4.67\right)^{3/2} \tag{14}$$

where D_* is a dimensionless particle diameter defined as:

$$D_* = D_n \sqrt[3]{\left(\frac{\rho_f}{\mu}\right)^2 g\left(\frac{\rho_p}{\rho_f} - 1\right)} \tag{15}$$

A more sophisticated approach was adopted by Y. Wang et al. (2018) based on multiple experiments with 13 spherical glass beads of 2.5 to 12 mm in diameter, and 133 carbonate particles of 2.9 to 9.7 mm of equivalent spherical diameter collected from a tropical reef in the South China Sea. The long, intermediate, and short axes were obatained using digital image analysis, and particle densities were measured individually. For calculation of the drag coefficient, Y. Wang et al. (2018) proposed:

$$C_D = 0.945 \frac{C_{D,sphere}}{\Psi^{\left(0.641 {Re_p}^{0.153}\right)}} {Re_p}^{-0.01} \tag{16}$$

where the drag coefficient for spheres is taken from Clift & Gauvin (1971):

$$C_{D,sphere} = \frac{24}{Re_p}\left(1 + 0.15 {Re_p}^{0.687}\right) + \frac{0.42}{\left(1 + \frac{42500}{{Re_p}^{1.16}}\right)} \tag{17}$$

and where Ψ is a complicated shape factor based on particle form and roundness, defined as the ratio

between sphericity Φ and inverse circularity X:

$$\Psi = \frac{\Phi}{X} = \frac{\left(\frac{A_{eq-sphere}}{A_{particle}}\right)}{\left(\frac{P_{particle}}{P_{eq-circle}}\right)} \quad (18)$$

where sphericity is the ratio of the surface area of the equivalent sphere and the surface area of the particle, and inverse circularity is the ratio of the perimeter of the maximum projection area and the perimeter of a circle with the surface area of the maximum projection area. Because the surface area of the particle (note: not the maximum projection area) is very difficult to determine in absence of micro-CT analysis, Y. Wang et al. (2018) approximated this parameter by taking the surface area of the bounding-box ellipsoid instead.

Finally, Riazi et al. (2020) split the drag coefficient into a 'laminar' and a 'turbulent' drag coefficient to account separately for frictional drag:

$$C_{D,f} = \left(\frac{9.50\mu}{{D_n}^{1.5}\rho_f\sqrt{g}} + 0.76\right)^{2.92} \quad (19)$$

and pressure drag:

$$C_{D,p} = \left(\frac{20.47\mu}{{D_n}^{1.5}\rho_f\sqrt{g}} + 1.02\right)^{-48.15} \quad (20)$$

Using the tropical carbonate dataset from Hawaii collected by Smith & Cheung (2003), they derived the following equation as the best fit:

$$w_t = \sqrt{\frac{11}{15}D_n g\left(\frac{\rho_p}{\rho_f} - 1\right)\frac{1}{C_{D,f} + C_{D,p}}CSF^{2/3}} \quad (21)$$

where CSF is Corey shape factor, and $C_{D,f}$ is the frictional drag coefficient in the laminar regime, and $C_{D,p}$ is the pressure drag coefficient in the turbulent regime.

6.2 Settling velocity using realistic particle models

In this section, the performance of previously proposed settling velocity equations for complex sediment particles of carbonate composition is tested. These equations were derived through the analysis of carbonate datasets comparable to the dataset used in this study. As input for the variables prompted by the equations of Alcérreca et al. (2013), Y. Wang et al. (2018), and Riazi et al. (2020), parameters obtained from the realistic particle models as measured by micro-CT in this study were used (Table 3). The quality of these settling velocity models is evaluated by inspecting the distribution of relative error between the settling velocity as predicted by the proposed equations and the value as observed in experiments.

The model of Alcérreca et al. (2013) prompts the nominal diameter ($D_n = \sqrt[3]{D_l D_i D_s}$; see Figure 3D) as the only dimensional variable. To test the performance of the equation using realistic particle models, the equivalent diameter ($D_{eq} = \sqrt[3]{(6/\pi)V_{meas}}$; see Figure 3C) derived from measured particle volume was used. The model of Alcérreca et al. (2013) overestimates the settling velocity of most complex carbonate particles in the dataset of this study with much variation, as shown by the broad scatter of data points and large errors (Figure 9A). Although the prediction of the settling velocity of spheroidal particles is more accurate, modelled settling velocity increasingly exceeds the observed value as particles become more ellipsoidal (see trend in data points colour-coded with CSF in Figure 9A), causing an asymmetric distribution of relative errors. This indicates that the settling velocity model of Alcérreca et al. (2013) does not account for particle shape.

The model of Y. Wang et al. (2018) is better at predicting settling velocity based on measured particle dimensions and fluid properties. Their complicated shape factor was calculated using the areas and perimeters as measured with micro-CT. High accuracy of the model is demonstrated by a close-to-zero mean μ of relative errors. However, the standard deviation σ of the relative errors is significant (Figure 9A). Although the distribution of relative error is symmetrical, Y. Wang et al. (2018) underestimate the settling velocity of spheroidal particles and overestimate the settling velocity of more ellipsoidal particles (see data points colour-coded with CSF in Figure 9A). Thus, also the model of Y. Wang et al. (2018) is not very capable of accounting for particle shape using measured parameters from the realistic particle model, despite its complicated shape factor.

Riazi et al. (2020) proposed an equation that with the parameters from the realistic model produces a narrower distribution of relative error, which is independent of particle ellipsoidity (i.e., there is no trend in relative error versus CSF as indicated by colour-coded data points in Figure 9A). The equation prompts the nominal diameter (D_n), which was substituted here with the equivalent diameter (D_{eq}) obtained from the

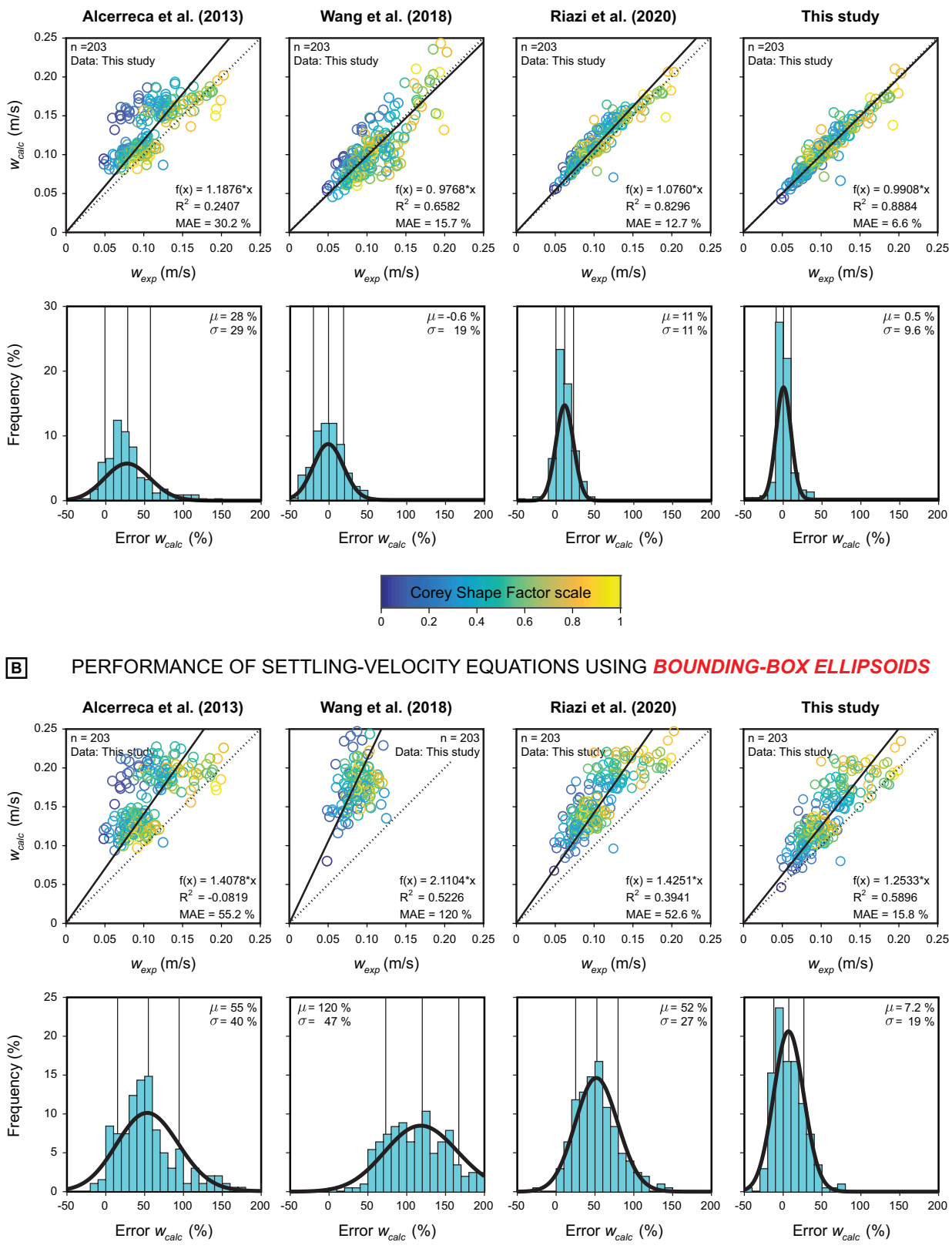

Figure 9 – Comparison of settling velocity equations for complex carbonate sediment particles. **(A)** Top row: Predicted settling velocities using dimensional parameters derived from realistic particle models obtained from micro-CT. Bottom row: Distribution of relative error for experimental versus calculated terminal settling velocity (Equation 12). **(B)** Top row: Predicted settling velocities using dimensional parameters derived from bounding-box ellipsoid particle models. Bottom row: Distribution of relative error for experimental versus calculated terminal settling velocity (Equation 12). Solid line is $f(x)$ representing the function of linear regression forced through the origin. Dashed line is the 1:1 relationship on which the calculated values exactly match the experimental values. *MAE* is mean absolute error (Equation 13). Probability density functions are normal-gamma distributions (Vaz & Fortes, 1988) for which mean μ (model accuracy) and standard deviation σ (model precision) are shown.

Table 3 – Dimensional variables applied in the calculation of settling velocity.

Study	Realistic particle model	Bounding-box ellipsoidal model
Alcérreca et al. (2013)	Equivalent diameter (D_{eq})	Nominal diameter (D_n)
Y. Wang et al. (2018)	Equivalent diameter (D_{eq}) Maximum projection area (A) Particle surface area[a]	Nominal diameter (D_n) Long, intermediate, and short diameters (D_s, D_i, D_l)[b,c]
Riazi et al. (2020)	Equivalent diameter (D_{eq}) Particle volume (V) Maximum projection area (A)	Nominal diameter (D_n) Long, intermediate, and short diameters (D_l, D_i, D_s)[d]
This study	Particle volume (V) Maximum projection area (A)	Short diameter (D_s)[e]

[a] This parameter is the surface area of the convex hull of the realistic particle model. Note that this parameter is different from the maximum projection area.
[b] Short, intermediate, and long diameters of the bounding-box ellipsoid are used to approximate the surface area of the ellipsoid.
[c] Intermediate and long diameters of the bounding-box ellipsoid are used to approximate the maximum projection area of the ellipsoid.
[d] Short, intermediate, and long diameters of the bounding-box ellipsoid are used to calculate Corey shape factor.
[e] Settling velocity is computed using calculated volume/area ratio of the bounding-box ellipsoid, which equals the short diameter multiplied by a factor $\frac{2}{3}$ (Table 2B).

realistic particle model, and *CSF* was calculated with the three particle axes. However, Riazi et al. (2020) overpredict settling velocity as reflected by the mean of the relative error distribution, which is shifted towards higher values.

Lastly, the simple settling velocity model generated in this study used the measured volume/area ratio as obtained from micro-CT (i.e., this is the same plot as in Figure 8). This study's model is slightly more precise compared to the settling velocity model of Riazi et al. (2020) and is characterised by a smaller standard deviation of relative error, indicating a lower degree of the scatter in data points. This study's model is also more accurate than any of the other models. In addition, there is no dependency of the error on particle shape, or more precisely: there is no dependency of the error on particle form, which is the first-order shape descriptor (i.e., second-order shape of particle angularity, and third-order shape of surface texture are not considered here; Griffiths, 1967; Barrett, 1980; see review in De Kruijf et al., 2021).

In conclusion, the model of Y. Wang et al. (2018) is accurate but not very precise (μ = –0.6 %, σ = 19 %), whereas the model of Riazi et al. (2020) is more precise but not very accurate (μ = 11 %, σ = 11 %). The Alcérreca et al. (2013) model performs poorly for the complex shapes of carbonate particles in the dataset of this study, as it solely relies on the nominal diameter to describe particle dimensions. The simple model constructed in this study has the accuracy of the model of Y. Wang et al. (2018) and the precision of the Riazi et al. (2020) model. Admittedly, the model in this study is generated with the same dataset that is used to evaluate its accuracy and precision. However, there currently exists no other dataset that provides the measured variables of complex sediment particles as prompted by the tested equations, for which also settling velocity was measured. The models of Alcérreca et al. (2013), Y. Wang et al. (2018), and Riazi et al. (2020) were built based on approximated parameters as obtained from ellipsoidal or spherical models rather than from measurements using realistic particle models. The effect of applying approximated values for particle dimensions is explored in the next section.

6.3 Settling velocity using bounding-box ellipsoids

In the previous section, the performance of existing settling velocity equations for complex carbonate particles was tested and compared using parameters derived from realistic particle models. In this section, the accuracy and precision of the settling velocity equations of Alcérreca et al. (2013), Y. Wang et al. (2018), and Riazi et al. (2020) are assessed by applying parameters derived from ellipsoidal particle models, based on which these equations were originally derived. Performance is evaluated from the distribution of relative error between the predicted and observed settling velocities (Figure 9B). The dimensional parameters obtained from the bounding-box ellipsoidal model are the approximated long,

intermediate, and short diameters of the particle (see Figure 3). The equations of Alcérreca et al. (2013), Y. Wang et al. (2018), and Riazi et al. (2020) all use the nominal diameter (i.e., the diameter of the nominal sphere, see Figure 3D) to perform part of the computation predicting the settling velocity. Y. Wang et al. (2018) and Riazi et al. (2020) also use the long, intermediate, and short particle axes to approximate areas and perimeters, and the Corey shape factor, respectively.

All these equations, including the equation modelled in this study, perform worse in predicting settling velocity of the sediment particles in the dataset based on dimensions extracted from the ellipsoidal model, compared to predictions based on dimensions derived from realistic particle models obtained from micro-CT. All equations return larger values of settling velocity than observed in experiments, which implies that particle weight (gravity force) in the equations is overrepresented and/or that friction is underrepresented in the settling velocity models. In other words, modelled particle volume is too large (see also Goossens, 1987) and/or modelled maximum projection area is too small. The significant deviations in the performance of settling velocity equations between measured and approximated dimensional particle parameters thus lie in the ability of the chosen particle model to represent volume/area ratio. However, if the mismatch between the true volume/area ratio and the volume/area ratio as returned by the ellipsoidal model is predictable, then, a correction factor could potentially be applied to ellipsoid dimensions. Volume/area ratios of natural sediment particles are further investigated in the next section.

7 Volumes and maximum projection area of natural sediment particles

The size and shape of natural sediment particles are fundamental properties in sedimentology and engineering. Together, particle volume and maximum projection area capture particle shape (represented by the first-order shape descriptor of particle form; see review in De Kruijf et al., 2021). These variables can be measured directly, for example using micro-CT and subsequent analysis of the digital models thus created (Carlson et al., 2003; Cnudde & Boone, 2013; Houghton et al., 2024; Maroof et al., 2020; Slootman et al., 2023; Yang et al., 2022). Classically, particle volume is determined by measuring the displaced volume of an individual grain submerged into a graduated volumetric pipette containing a known fluid volume (Corey, 1949; Schulz, 1954; Wilde, 1952). Maximum projection area is commonly determined with digital image analysis (static image analysis: Al-Rousan et al., 2007; Alcérreca et al., 2013; Buckland et al., 2021; Buscombe et al., 2010; Dioguardi & Mele, 2015; Mao et al., 2023, or dynamic image analysis: Patchigolla & Wilkinson, 2009; Zhang et al., 2021). In any case, the direct measurement of particle volume and maximum projection area is rather complicated and laborious (Blott & Pye, 2008). It is much easier to obtain the axial dimensions of sediment particles, and then calculate the volume and maximum projection area of the bounding-box ellipsoid, as is common practice in literature (Baba & Komar, 1981; Komar & Reimers, 1978; Smith & Cheung, 2003). However, as demonstrated above, volumes are larger and/or maximum projection areas are smaller in the ellipsoidal models than in the realistic particle models. To evaluate if there exists a predictable mismatch between modelled and actual dimensional particle parameters, an extensive literature survey was conducted compiling publications on sediments that report realistic particle volumes and maximum projection areas, and which in addition document the long, intermediate, and short axes of those particles to enable the approximation of ellipsoidal volume and maximum projection area.

The compilation comprises 27 datasets from twelve studies reporting a total of 3 622 particles, including skeletal carbonates, siliciclastics, volcaniclastics, plastic particles, rock crusher fragments (simulating freshly weathered siliciclastic particles), and sedimentary gold grains (Table S2 in supplementary materials). Volume was measured for most of the datasets, whereas maximum projection area was measured for only eight datasets. The large carbonate dataset of Alcérreca et al. (2013) (1 557 grains) has a large control on the number of particles in the compilation, as it contains area measurements but lacks volume data. Only six datasets from three studies document both measured volume and maximum projection area that allows for direct comparison of measured versus calculated volume/area ratios.

Error analysis was carried out for all measured versus calculated values per dataset (Figure 10, see also Figures S1–S3 in supplementary materials). The means and standard deviations of normal-gamma

distributions of the relative error were determined (Table S2 in supplementary materials) and are shown in the bivariate plots in Figure 10. Each dataset is represented by a circle. The centre of the circle lies at the combination of the mean and standard deviation, while the size of the circle indicates the number of particles in the dataset. The mean of the relative error represents the accuracy with which the calculated value approximates the measured value, i.e., the mean is a measure of how 'correct' the ellipsoidal parameter is in estimating the actual particle dimensions of volume, maximum projection area, and volume/area ratio. The standard deviation of the relative error reflects the precision of the ellipsoidal approximations, i.e., standard deviation is a measure of the variability in the calculated values.

Most of the calculated volumes obtained from ellipsoidal models are larger than the measured particle volumes (Figure 10A). Datasets with larger over-estimations also show broader variations in relative error between calculated and measured particle volumes. The three carbonate datasets that report measured volume are among the datasets with the highest means of relative error distribution, implying that the ellipsoidal model is more appropriate for approximating particle volume for siliciclastic particles than for carbonate grains. The only carbonate study that used micro-CT to obtain particle volumes is this study, which displays the highest relative errors for calculated versus measured volumes in terms of both accuracy and precision.

The much smaller compilation of datasets reporting measured maximum projection areas reveals a trend opposite to that of volume (Figure 10B). The carbonate datasets are more accurate than the siliciclastic datasets and are generally accompanied by higher precision. This trend is not self-evident, as it is unclear why ellipsoids would present more accurate and more precise approximations of actual maximum projection area for carbonate particles than for siliciclastics.

Finally, no more than six datasets from three studies have measured both particle volume and maximum projection area (Figure 10C). The two carbonate studies plot close to each other, demonstrating large (c. 75 %) means of overestimation of particle volume/area ratios with a broad spread in relative error. The relative errors of the four siliciclastic datasets have narrower distributions, and generally underestimate volume/area ratios.

It is tempting to conclude that ellipsoidal models largely overestimate particle volume of carbonate grains, more so than for particles of siliciclastic composition, and that this trend is opposite for maximum projection area. However, there might be large variations between datasets. Even if belonging to similar compositions in terms of siliciclastic or carbonate, there exist significant differences between carbonate depositional environments, and similarly between siliciclastic ones. In addition, these compilations are most likely too small for conclusions on definitive trends based on composition. The number of studies that measured both particle volume and maximum projection area is even smaller, and the number of particles contained in them is low.

Although there are hints that siliciclastic particles are more accurately represented by ellipsoids than carbonate grains, large compilations have shown that natural sediment grains are not well-represented by ellipsoids (see *Part 1*, Slootman et al., 2026). At present, there are insufficient data available to constrain whether there are predictable trends between actual volume/area ratios of sediment particles and ellipsoidal models constructed based on the long, intermediate, and short particle axes. If there are correction factors to modify ellipsoid dimensions to obtain actual particle volume/area ratios, then this must be demonstrated with large compilations of significant datasets that cover the broad range of depositional environments capturing the variations in particle composition and shape.

8 Discussion

The settling velocity of particles has wide applications in earth sciences and engineering. A sediment particle undergoes initial acceleration until a balance of forces is reached between submerged weight and friction with the fluid (Wadell, 1934), which are respectively a function of particle volume and maximum projection area. Solving this equilibrium for settling velocity reveals that the dependent length variable in this problem is the volume/area ratio of the particle (Table 2). For spheres, the volume/area ratio is captured by its diameter. Mathematical relationships between the volume and maximum projection area of ellipsoids demonstrate that the settling velocity of an ellipsoid is instead controlled by its shortest

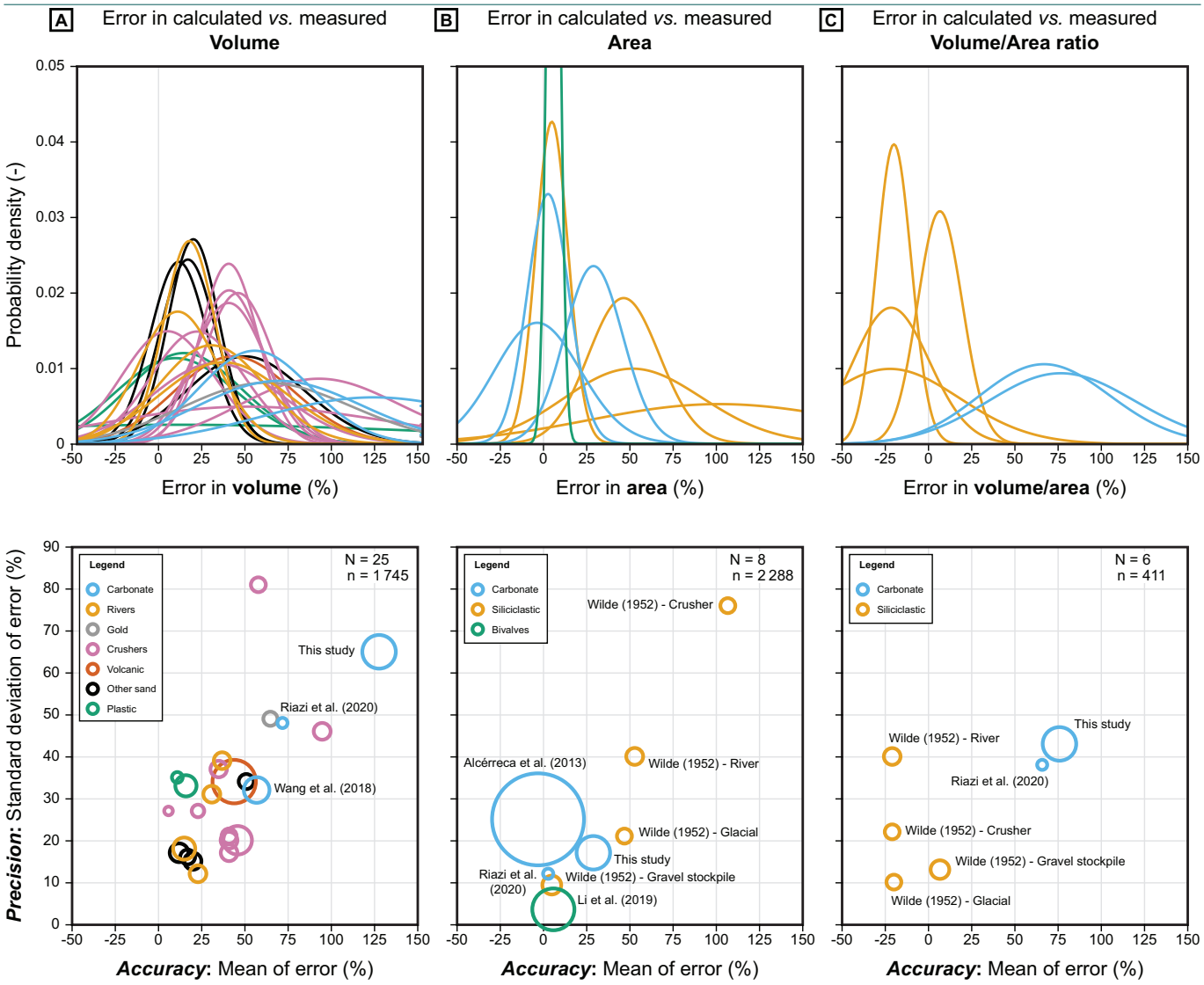

Figure 10 – Error between calculated and measured dimensional parameters of sediment particles. Calculated parameters represent approximations using the bounding-box ellipsoidal model based on the long, intermediate, and short axes as reported in literature. Measured parameters of those same particles were obtained using laboratory techniques by the referenced authors. **(A)** Particle volume. **(B)** Maximum projection area. **(C)** Volume/area ratio, which was only possible to determine if both measured volume and area were documented. *N* and *n* indicate the number of datasets and combined number of particles, respectively. Circle sizes are scaled between the plots and correspond to the number of particles in that dataset. Probability density functions are normal-gamma distributions (Vaz & Fortes, 1988). See Table S2 for overview of datasets and Figures S1-S3 in the supplementary materials for the values used to perform the error analyses.

diameter (see also Riazi & Türker, 2019). Despite these fundamental insights – which have long been known – most studies on settling velocity work with a spherical diameter (Figure 3, e.g. Cahyono, 2022; Dietrich, 1982; Ferguson & Church, 2004; Gibbs et al., 1971; Jiménez & Madsen, 2003; Komar & Reimers, 1978; Wu & Wang, 2006).

Analytical solutions for settling velocity exist for both laminar and fully turbulent flow regimes for spheres (DallaValle, 1948; Stokes, 1850) and ellipsoids (Oberbeck, 1876). However, settling velocity equations for spheres in the transitional regime require an empirical approach (e.g., Clift & Gauvin, 1971). Since natural sediments are not of perfect geometric shape, the common approach for these particles is to adapt empirical settling equations for spheres by the introduction of a shape factor. Upon the assumption that sediment particles are best described as ellipsoids (e.g., Riazi et al., 2020; Smith & Cheung, 2003), studies commonly apply the Corey shape factor as a measure of ellipsoidity in their settling model. Using spherical diameter to account for size, and Corey shape factor to specify shape, significant emphasis is placed on the short diameter of the ellipsoidal particle model (e.g., in a linear relationship $D_n\,CSF = D_l D_i D_s \left(D_s/\sqrt{D_l D_i}\right) = D_s{}^2\sqrt{D_l D_i}$). A reasonable fit between calculated and experimental settling velocity is thus found because this method approximates

the ellipsoidal model by using D_s as the length variable, but not quite so. In addition, the Corey shape factor cannot discriminate between different ellipsoids as demonstrated by the crossing of *CSF*-isolines through the flatness-elongation diagram of Zingg (1935) (Figure 4B). However, *CSF*-isolines are roughly parallel with isolines of ellipsoidal maximum projection area (see De Kruijf et al., 2021, Figure 14), which may explain some of the correlation found when using the Corey shape factor. To compensate for the mismatch between the predicted and observed settling velocity due to employing the Corey shape factor, or a similar ellipsoidal model, additional coefficients are inserted into settling velocity equations, such as particle angularity (e.g., Powers, 1953 roundness; in Dietrich, 1982) or combined parameters (e.g., mass-to-projected area ratio in Duperron et al., 2025) or sediment-specific parameters (e.g., shape descriptors in Ferguson & Church, 2004; and the alpha-constant in Riazi & Türker, 2019). However, this added complexity further removes the settling velocity model from being universal, which should be the ultimate objective.

The contribution of this paper is to propose a universal *approach*, rather than the discussion of yet another equation, for the settling velocity of irregular sediment particles. We acknowledge that the linear relationship between particle Reynolds number and drag coefficient on a log-log scale, as used in this approach, entails limitations to application outside of the transitional regime. However, this is a shortcoming that can be solved by fitting the relationship with a more sophisticated equation. Hence, the universality of the volume/area ratio as a combined particle size-shape parameter remains valid. Volume/area ratio as the dependent length variable in the settling problem performs better than any method based on the ellipsoidal model as approximation of particle size and shape (see *Part 1,* Slootman et al., 2026). Perhaps, the mismatch between the ellipsoidal model and the actual particle dimensions is predictable, with correction factors that can be applied to sediment particles from specific depositional environments. Skeletal remains in biota-specific habitats (e.g., Musso et al., 2025) or deposits in carbonate sub-environments (e.g., reef, fore reef, back reef, and lagoon) each have their own particle production and distribution characteristics (e.g., Lokier et al., 2013; and Purser, 1973 for carbonate ramps; Ginsburg, 1956; and Reijmer et al., 2009 for flat-topped systems). Such a facies-specific approach might require better reconstruction of particle volumes and maximum projection areas, for example as obtained from micro-CT. However, there are currently not enough data to demonstrate this, which opens avenues for future research. The ability to better predict particle settling velocity, especially for irregular skeletal carbonate grains, enables improved understanding of source-to-sink processes in carbonate platform settings (e.g., Morgan & Kench, 2016).

9 Conclusions

Settling velocity of sediment particles is a function of the ratio between particle volume and maximum projection area. This length parameter captures both size and shape of the sediment grain. Because longest, intermediate, and shortest particle diameters are relatively easy to obtain, the ellipsoidal model is a popular representation of sediment grains. However, ellipsoids offer poor approximations of natural sediment particles, especially if these are irregular in nature such as skeletal carbonates. Hence, as shown here, settling velocity models that use spherical diameters and an ellipsoidal shape factor underperform compared to equations that employ a realistic volume/area ratio. Accurate determination of particle volume and maximum projection area requires more advanced techniques such as micro-computed tomography. There are currently insufficient data to explore whether the actual volume/area ratio of sediment particles can be predicted from their principal axes.

Acknowledgements

Dr. Alcérreca, Dr. Wang, and Prof. Cheung are thanked for sharing the unpublished data used in their publications. The use of the micro-CT facility at the College of Petroleum Engineering and Geosciences at King Fahd University of Petroleum & Minerals (Dhahran, KSA) is greatly appreciated. We are indebted to Prof. Pierre Weill and Dr. Siddhi Joshi for their careful reviews of our manuscript. Associate Editor Dr. Siddhi Joshi and Executive Editor Prof. Murray Gingras are acknowledged for their efforts in coordinating the review process. We thank Dr. Jarred Lloyd, production manager of Sedimentologika, for his assistance in refining the presentation of our paper.

Data and code availability

Table S1 contains all the particle data from the micro-CT dataset used in this study. Table S2 comprises the volume and area of particles measured in other studies. Also

included are the MATLAB scripts used to plot the figures in this paper.

Supplementary materials

Supplementary material to this article can be found online at: doi:10.57035/journals/sdk.2026.e41.2307

Conflict of interest statement

The authors declare they do not have any tangible or perceived conflicts of interest with regard to this research.

Artificial intelligence use statement

All research, analysis, writing, and editing were performed without generative AI assistance.

Funding

The authors received no specific funding for this work.

Citing this Research Article

To cite this paper use the following information:

Authors
Arnoud Slootman, Max de Kruijf, Guenther Glatz, Joris T. Eggenhuisen, Zane R. Jobe, John J. G. Reijmer

Title
Settling velocity of sediment grains, Part 2: Volume/area ratio as descriptor of particle size and shape in sediment hydrodynamics

Short Title
Settling velocity: Volume/area ratio as descriptor of particle size and shape

Publishing Information
Publication: Sedimentologika
Volume: 4
Issue: 1
Year: 2026
DOI: 10.57035/journals/sdk.2026.e41.2307
Language: en

Appendix A

Table A1 – Symbols and descriptions of parameters used in equations in this article.

Symbol	Description
A	Particle maximum projection area
A_{calc}	Calculated particle maximum projection area
$A_{eq-sphere}$	Surface area of the equivalent sphere (Y. Wang et al. 2018)
A_{meas}	Measured particle maximum projection area
$A_{particle}$	Surface area of the particle (Y. Wang et al. 2018)
$abs(\varepsilon)$	Absolute error
C_D	Drag coefficient
$C_{D,exp}$	Experimental drag coefficient
$C_{D,f}$	Frictional drag coefficient in the laminar regime (Riazi et al. 2020)
$C_{D,p}$	Pressure drag coefficient in the turbulent regime (Riazi et al. 2020)
$C_{D,sphere}$	Drag coefficient for spheres
CSF	Corey shape factor
D_{eq}	Equivalent particle diameter
D_i	Intermediate particle diameter
D_l	Long particle diameter
D_n	Nominal particle diameter
D_s	Short particle diameter
D_*	Dimensionless particle diameter (Alcérreca et al. 2013)
$f(\square)$	Function of the variable(s) between parentheses
F_b	Buoyant force
F_D	Drag force
F_g	Weight (force of gravity)
F_g'	Submerged weight
g	Gravitational acceleration
i	Index counting iterations
L	Particle length parameter
MAE	Mean absolute error
n	Number of measurements
$P_{eq-circle}$	Perimeter of a circle with the surface area of the maximum area (Y. Wang et al. 2018)
$P_{particle}$	Perimeter of the maximum projection area (Y. Wang et al. 2018)
Re_p	Particle Reynolds number
V	Particle volume
V_{calc}	Measured particle volume
V_{meas}	Calculated particle volume
$\left(\frac{V}{A}\right)_{calc}$	Calculated ratio between particle volume and particle maximum projection area
$\left(\frac{V}{A}\right)_{meas}$	Measured ratio between particle volume and particle maximum projection area
w	Settling velocity
w_t	Terminal settling velocity
$w_{t,calc}$	Calculated terminal settling velocity

Table A1 continued

Symbol	Description
$w_{t,exp}$	Experimental terminal settling velocity (observed)
ε	Relative error
μ	Dynamic fluid viscosity
μ	Mean (model accuracy)
ρ_f	Fluid density
ρ_p	Particle density
σ	Standard deviation (model precision)
Φ	Particle sphericity (Y. Wang et al. 2018)
X	Particle inverse circularity (Y. Wang et al. 2018)
Ψ	Shape factor of Y. Wang et al. (2018)

References

Ahrens, J. P. (2003). Simple Equations to Calculate Fall Velocity and Sediment Scale Parameter. *Journal of Waterway, Port, Coastal, and Ocean Engineering*, *129*(3), 146–150. https://doi.org/10.1061/(ASCE)0733-950X(2003)129:3(146)

Al-Rousan, T., Masad, E., Tutumluer, E., & Pan, T. (2007). Evaluation of image analysis techniques for quantifying aggregate shape characteristics. *Construction and Building Materials*, *21*(5), 978–990. https://doi.org/10.1016/j.conbuildmat.2006.03.005

Alcérreca, J. C., Silva, R., & Mendoza, E. (2013). Simple settling velocity formula for calcareous sand. *Journal of Hydraulic Research*, *51*(2), 215–219. https://doi.org/10.1080/00221686.2012.753645

Anders, M. H., Krueger, S. W., & Sadler, P. M. (1987). A New Look at Sedimentation Rates and the Completeness of the Stratigraphic Record. *The Journal of Geology*, *95*(1), 1–14. https://doi.org/10.1086/629103

Baba, J., & Komar, P. D. (1981). Settling Velocities of Irregular Grains at Low Reynolds Numbers. *Journal of Sedimentary Research*, *51*(1), 121–128. https://doi.org/10.1306/212f7c25-2b24-11d7-8648000102c1865d

Bagheri, G. H., & Bonadonna, C. (2016). On the drag of freely falling non-spherical particles. *Powder Technology*, *301*, 526–544. https://doi.org/10.1016/j.powtec.2016.06.015

Bagheri, G. H., Bonadonna, C., Manzella, I., & Vonlanthen, P. (2015). On the characterization of size and shape of irregular particles. *Powder Technology*, *270*, 141–153. https://doi.org/10.1016/j.powtec.2014.10.015

Barrett, P. J. (1980). The shape of rock particle, a critical review. *Sedimentology*, *27*, 291–303. https://doi.org/10.1111/j.1365-3091.1980.tb01179.x

Bian, C., Chen, J., Jiang, C., Wu, Z., & Yao, Z. (2023). Threshold of motion of coral reef sediment under currents in flume experiments. *Sedimentology*, *70*(6), 1723–1740. https://doi.org/10.1111/sed.13082

Blott, S. J., & Pye, K. (2008). Particle shape: A review and new methods of characterization and classification. *Sedimentology*, *55*(1), 31–63. https://doi.org/10.1111/j.1365-3091.2007.00892.x

Brown, A. G., Carey, C., Erkens, G., Fuchs, M., Hoffmann, T., Macaire, J.-J., Moldenhauer, K.-M., & Walling, D. E. (2009). From sedimentary records to sediment budgets: Multiple approaches to catchment sediment flux. *Geomorphology*, *108*(1–2), 35–47. https://doi.org/10.1016/j.geomorph.2008.01.021

Buckland, H. M., Saxby, J., Roche, M., Meredith, P., Rust, A. C., Cashman, K. V., & Engwell, S. L. (2021). Measuring the size of non-spherical particles and the implications for grain size analysis in volcanology. *Journal of Volcanology and Geothermal Research*, *415*, 107257. https://doi.org/10.1016/j.jvolgeores.2021.107257

Buscombe, D., Rubin, D. M., & Warrick, J. A. (2010). A universal approximation of grain size from images of noncohesive sediment. *Journal of Geophysical Research: Earth Surface*, *115*(F2), 2009JF001477. https://doi.org/10.1029/2009JF001477

Cahyono, M. (2022). The Development of Explicit Equations for Estimating Settling Velocity Based on Artificial Neural Networks Procedure. *Hydrology*, *9*(6), 98. https://doi.org/10.3390/hydrology9060098

Camenen, B. (2007). Simple and General Formula for the Settling Velocity of Particles. *Journal of Hydraulic Engineering*, *133*(2), 229–233. https://doi.org/10.1061/(asce)0733-9429(2007)133:2(229)

Camenen, B., Bayram, A., & Larson, M. (2006). Equivalent Roughness Height for Plane Bed under Steady Flow. *Journal of Hydraulic Engineering*, *132*(11), 1146–1158. https://doi.org/10.1061/(ASCE)0733-9429(2006)132:11(1146)

Carlson, W. D., Rowe, T., Ketcham, R. A., & Colbert, M. W. (2003). Applications of high-resolution X-ray computed tomography in petrology, meteoritics and palaeontology. *Geological Society, London, Special Publications*, *215*(1), 7–22. https://doi.org/10.1144/GSL.SP.2003.215.01.02

Cheng, N.-S. (1997). Simplified Settling Velocity Formula for Sediment Particle. *Journal of Hydraulic Engineering*, *123*(2), 149–152. https://doi.org/10.1061/(ASCE)0733-9429(1997)123:2(149)

Clift, R., & Gauvin, W. H. (1971). Motion of entrained particles in gas streams. *Canadian Journal of Chemical Engineering*, *49*(4), 439–448. https://doi.org/10.1002/cjce.5450490403

Clift, R., Grace, J. R., & Weber, M. E. (1978). *Bubbles, drops, and particles*. Academic Press.

Cnudde, V., & Boone, M. N. (2013). High-resolution X-ray computed tomography in geosciences: A review of the current technology and applications. *Earth-Science Reviews*, *123*, 1–17. https://doi.org/10.1016/j.earscirev.2013.04.003

Collins, M. B., & Rigler, J. K. (1982). The use of settling velocity in defining the initiation of motion of heavy mineral grains, under unidirectional flow. *Sedimentology*, *29*(3), 419–426. https://doi.org/10.1111/j.1365-3091.1982.tb01804.x

Corey, A. T. (1949). *Influence of shape on the fall velocity of sand grains* [Master thesis, Colorado Agricultural and Mechanical College]. https://doi.org/10.25675/3.025499

DallaValle, J. M. (1948). *Micromeritics – The Technology Of Fine Particles* (2nd ed.). Pitman Publishing Co. https://hdl.handle.net/2027/wu.89080444581

De Kruijf, M., Slootman, A., De Boer, R. A., & Reijmer, J. J. G. (2021). On the settling of marine carbonate grains: Review and challenges. *Earth-Science Reviews*, *January*, 103532–103532. https://doi.org/10.1016/j.earscirev.2021.103532

Dey, S., & Ali, S. Z. (2019). Bed sediment entrainment by streamflow: State of the science. *Sedimentology*, *66*(5), 1449–1485. https://doi.org/10.1111/sed.12566

Dey, S., Ali, S. Z., & Padhi, E. (2019). Terminal fall velocity: the legacy of Stokes from the perspective of fluvial hydraulics. *Proceedings of the Royal Society A: Mathematical, Physical and Engineering Sciences*, *475*(2228), 20190277. https://doi.org/10.1098/rspa.2019.0277

Dietrich, W. E. (1982). Settling velocity of natural particles. *Water Resources Research*, *18*(6), 1615–1626. https://doi.org/10.1029/WR018i006p01615

Dioguardi, F., & Mele, D. (2015). A new shape dependent drag correlation formula for non-spherical rough particles. Experiments and results. *Powder Technology*, *277*, 222–230. https://doi.org/10.1016/j.powtec.2015.02.062

Duperron, M., Mouazé, D., Weill, P., Tessier, B., & Scasso, R. A. (2025). Hydrodynamic behaviour of organo-phosphatic bioclastic sediments: An experimental study on linguliform brachiopod shell fragments. *Sedimentology*, *72*(4), 1343–1368. https://doi.org/10.1111/sed.70005

Egiazaroff, I. V. (1965). Calculation of Nonuniform Sediment Concentrations. *Journal of the Hydraulics Division*, *91*(4), 225–247. https://doi.org/10.1061/JYCEAJ.0001277

Fennessey, L. A. J., & Jarrett, A. R. (1994). The dirt in a hole: A review of sedimentation basins for urban areas and construction sites. *Journal of Soil and Water Conservation*, *49*(4), 317–323. https://doi.org/10.1080/00224561.1994.12456871

Ferguson, R. I., & Church, M. (2004). A simple universal equasion for grain settling velosity. *Journal of Sedimentary Research*, *74*(6), 933–937. https://doi.org/10.1306/051204740933

Flemming, N. C. (1965). Form and Function of Sedimentary Particles. *Journal of Sedimentary Research*, *35*(2), 381–390. https://doi.org/10.1306/74D71280-2B21-11D7-8648000102C1865D

Fornberg, B. (1988). Steady viscous flow past a sphere at high Reynolds numbers. *Journal of Fluid Mechanics*, *190*, 471–489. https://doi.org/10.1017/S0022112088001417

Gibbs, R. J., Matthews, M. D., & Link, D. A. (1971). The Relationship Between Sphere Size And Settling Velocity. *Journal of Sedimentary Research*, *41*(1), 7–18. https://doi.org/10.1306/74D721D0-2B21-11D7-8648000102C1865D

Ginsburg, R. N. (1956). Environmental Relationships of Grain Size and Constituent Particles in Some South Florida Carbonate Sediments. *AAPG Bulletin*, *40*(10), 2384–2427. https://doi.org/10.1306/5CEAE598-16BB-11D7-8645000102C1865D

Göğüş, M., İpekç, O. N., & Kökpinar, M. A. (2001). Effect of Particle Shape on Fall Velocity of Angular Particles. *Journal of Hydraulic Engineering*, *127*(10), 860–869. https://doi.org/10.1061/(ASCE)0733-9429(2001)127:10(860)

Goossens, D. (1987). A drag coefficient equation for natural, irregularly shaped particles. *Catena*, *14*(1–3), 73–99. https://doi.org/10.1016/S0341-8162(87)80007-3

Griffiths, J. C. (1967). *Scientific Method in Analysis of Sediments*. McGraw-Hill.

Hayes, C. T., Costa, K. M., Anderson, R. F., Calvo, E., Chase, Z., Demina, L. L., Dutay, J.-C., German, C. R., Heimbürger-Boavida, L.-E., Jaccard, S. L., Jacobel, A., Kohfeld, K. E., Kravchishina, M. D., Lippold, J., Mekik, F., Missiaen, L., Pavia, F. J., Paytan, A., Pedrosa-Pamies, R., … Zhang, J. (2021). Global Ocean Sediment Composition and Burial Flux in the Deep Sea. *Global Biogeochemical Cycles*, *35*(4), e2020GB006769. https://doi.org/10.1029/2020GB006769

Hjulström, F. (1935). Studies in the morphological activity of rivers as illustrated by the river Fyris. *Bulletin Geological Institute Uppsala*, *XXV*, 221–527.

Houghton, J. E., Behnsen, J., Duller, R. A., Nichols, T. E., & Worden, R. H. (2024). Particle size analysis: A comparison of laboratory-based techniques and their application to geoscience. *Sedimentary Geology*, *464*, 106607. https://doi.org/10.1016/j.sedgeo.2024.106607

Jiménez, J. A., & Madsen, O. S. (2003). A Simple Formula to Estimate Settling Velocity of Natural Sediments. *Journal of Waterway, Port, Coastal, and Ocean Engineering*, *129*(2), 70–78. https://doi.org/10.1061/(ASCE)0733-950X(2003)129:2(70)

Komar, P. D., & Reimers, C. E. (1978). Grain Shape Effects on Settling Rates. *Journal of Geology*, *86*(2), 193–209. https://doi.org/10.1086/649674

Kondolf, G. M., Gao, Y., Annandale, G. W., Morris, G. L., Jiang, E., Zhang, J., Cao, Y., Carling, P., Fu, K., Guo, Q., Hotchkiss, R., Peteuil, C., Sumi, T., Wang, H., Wang, Z., Wei, Z., Wu, B., Wu, C., & Yang, C. T. (2014). Sustainable sediment management in reservoirs and regulated rivers: Experiences from five continents. *Earth's Future*, *2*(5), 256–280. https://doi.org/10.1002/2013EF000184

Krumbein, W. C. (1941). The Effects of Abrasion on the Size, Shape and Roundness of Rock Fragments. *Journal of Geology*, *49*(5), 482–520. https://doi.org/10.1086/624985

Le Roux, J. P. (2005). Grains in motion: A review. *Sedimentary Geology*, *178*(3–4), 285–313. https://doi.org/10.1016/j.sedgeo.2005.05.009

Li, L., Ni, J., Chang, F., Yue, Y., Frolova, N., Magritsky, D., Borthwick, A. G. L., Ciais, P., Wang, Y., Zheng, C., & Walling, D. E. (2020). Global trends in water and sediment fluxes of the world's large rivers. *Science Bulletin*, *65*(1), 62–69. https://doi.org/10.1016/j.scib.2019.09.012

Lokier, S. W., Knaf, A., & Kimiagar, S. (2013). A quantitative analysis of Recent arid coastal sedimentary facies from the Arabian Gulf Coastline of Abu Dhabi, United Arab Emirates. *Marine Geology*, *346*, 141–152. https://doi.org/10.1016/j.margeo.2013.09.006

Mao, L., Li, J., Shimozono, T., & Tajima, Y. (2023). Impacts of Particle Shape, Skeletal Porosity and Density on the Settling Velocity of Gravel-Size Coral Debris. *Journal of Geophysical Research: Earth Surface*, *128*(5), e2022JF006996. https://doi.org/10.1029/2022JF006996

Maroof, M. A., Mahboubi, A., Noorzad, A., & Safi, Y. (2020). A new approach to particle shape classification of granular materials. *Transportation Geotechnics*, *22*, 100296. https://doi.org/10.1016/j.trgeo.2019.100296

Middleton, G. V., & Southard, J. B. (Eds.). (1984). *Mechanics of Sediment Movement: Vol. SEPM Short Course Notes: 3*. SEPM Society for Sedimentary Geology. https://doi.org/10.2110/scn.84.03

Miedema, S. A. (2010). Constructing the shields curve, a new theoretical approach and its applications. In J. Dobson (Ed.), *Proceedings of the 19th world dredging congress* (pp. 732–750). Chida. https://www.researchgate.net/publication/228750218

Morgan, K. M., & Kench, P. S. (2016). Reef to island sediment connections on a Maldivian carbonate platform: using benthic ecology and biosedimentary depositional facies to examine island-building potential. *Earth Surface Processes and Landforms*, *41*(13), 1815–1825. https://doi.org/10.1002/esp.3946

Musso, M. S., Slootman, A., Wood, L. J., & Jobe, Z. R. (2025). Stalked crinoids: From skeleton to sediment. *Journal of Sedimentary Research*, *95*(6), 1056–1062. https://doi.org/10.2110/jsr.2025.099

Oberbeck, A. (1876). Ueber stationäre Flüssigkeitsbewegungen mit Berücksichtigung der inneren Reibung. *Journal Für Die Reine Und Angewandte Mathematik*, *1876*(81), 62–80. https://doi.org/10.1515/crll.1876.81.0

Paola, C., Straub, K., Mohrig, D., & Reinhardt, L. (2009). The "unreasonable effectiveness" of stratigraphic and geomorphic experiments. *Earth-Science Reviews*, *97*(1–4), 1–43. https://doi.org/10.1016/j.earscirev.2009.05.003

Paphitis, D., Collins, M. B., Nash, L. A., & Wallbridge, S. (2002). Settling velocities and entrainment thresholds of biogenic sands (shell fragments) under unidirectional flow. *Sedimentology*, *49*(1), 211–225. https://doi.org/10.1046/j.1365-3091.2002.00446.x

Parrinello, G., & Kondolf, G. M. (2021). The social life of sediment. *Water History*, *13*(1), 1–12. https://doi.org/10.1007/s12685-021-00280-w

Patchigolla, K., & Wilkinson, D. (2009). Crystal Shape Characterisation of Dry Samples using Microscopic and Dynamic Image Analysis. *Particle & Particle Systems Characterization*, *26*(4), 171–178. https://doi.org/10.1002/ppsc.200700030

Peregrine, D. H. (1985). A note on the steady high-Reynolds-number flow about a circular cylinder. *Journal of Fluid Mechanics*, *157*, 493–500. https://doi.org/10.1017/S0022112085002464

Powers, M. C. (1953). A new roundness scale for sedimentary particles. *Journal of Sedimentary Research*, *23*(2), 117–119. https://doi.org/10.1306/d4269567-2b26-11d7-8648000102c1865d

Prager, E. J., Southard, J. B., & Vivoni-Gallart, E. R. (1996). Experiments on the entrainment threshold of well-sorted and poorly sorted carbonate sands. *Sedimentology*, *43*(1), 33–40. https://doi.org/10.1111/j.1365-3091.1996.tb01457.x

Purser, B. H. (1973). Sedimentation around Bathymetric Highs in the Southern Persian Gulf. In B. H. Purser (Ed.), *The Persian Gulf* (pp. 157–177). Springer. https://doi.org/10.1007/978-3-642-65545-6_9

Reijmer, J. J. G. (2021). Marine carbonate factories: Review and update. *Sedimentology*, *68*(5), 1729–1796. https://doi.org/10.1111/sed.12878

Reijmer, J. J. G., Swart, P. K., Bauch, T., Otto, R., Reuning, L., Roth, S., & Zechel, S. (2009). A Re-Evaluation of Facies on Great Bahama Bank I: New Facies Maps of Western Great Bahama Bank. In P. K. Swart, G. P. Eberli, J. A. McKenzie, I. Jarvis, & T. Stevens (Eds.), *Perspectives in carbonate geology* (1st ed., pp. 29–46). Wiley. https://doi.org/10.1002/9781444312065.ch3

Reynolds, O. (1883). XXIX. An experimental investigation of the circumstances which determine whether the motion of water shall be direct or sinuous, and of the law of resistance in parallel channels. *Philosophical Transactions of the Royal Society of London*, *174*, 935–982. https://doi.org/10.1098/rstl.1883.0029

Riazi, A., & Türker, U. (2019). The drag coefficient and settling velocity of natural sediment particles. *Computational Particle Mechanics*, *6*(3), 427–437. https://doi.org/10.1007/s40571-019-00223-6

Riazi, A., Vila-Concejo, A., Salles, T., & Türker, U. (2020). Improved drag coefficient and settling velocity for carbonate sands. *Scientific Reports*, *10*(1), 9465. https://doi.org/10.1038/s41598-020-65741-3

Rieux, A., Weill, P., Mouaze, D., Poirier, C., Nechenache, F., Perez, L., & Tessier, B. (2019). Threshold of motion and settling velocities of mollusc shell debris: Influence of faunal composition. *Sedimentology*, *66*(3), 895–916. https://doi.org/10.1111/sed.12521

Rott, N. (1990). Note on the History of the Reynolds Number. *Annual Review of Fluid Mechanics*, *22*(1), 1–12. https://doi.org/10.1146/annurev.fl.22.010190.000245

Schlager, W. (2003). Benthic carbonate factories of the Phanerozoic. *International Journal of Earth Sciences*, *92*(4), 445–464. https://doi.org/10.1007/s00531-003-0327-x

Schleiss, A. J., Franca, M. J., Juez, C., & De Cesare, G. (2016). Reservoir sedimentation. *Journal of Hydraulic Research*, *54*(6), 595–614. https://doi.org/10.1080/00221686.2016.1225320

Schlichting, H. (1975). *Boundary-Layer Theory* (7th ed.). McGraw-Hill.

Schulz, E. F. (1954). *Effect of shape on the fall velocity of sand particles* [Master thesis]. Colorado Agricultural and Mechanical College.

Slootman, A., De Boer, P. L., Cartigny, M. J. B., Samankassou, E., & Moscariello, A. (2019). Evolution of a carbonate delta generated by gateway-funnelling of episodic currents. *Sedimentology*, *66*(4), 1302–1340. https://doi.org/10.1111/sed.12585

Slootman, A., de Kruijf, M., Glatz, G., Eggenhuisen, J. T., Jobe, Z. R., & Reijmer, J. J. G. (2026). Settling velocity of sediment grains, Part 1: Natural sediment particles are not ellipsoids. *Sedimentologika*, *4*(1). https://doi.org/10.57035/journals/sdk.2026.e41.1937

Slootman, A., de Kruijf, M., Glatz, G., Eggenhuisen, J. T., Zühlke, R., & Reijmer, J. J. G. (2023). Shape-dependent settling velocity of skeletal carbonate grains: Implications for calciturbidites. *Sedimentology*, *70*(6), 1683–1722. https://doi.org/10.1111/sed.13103

Smith, D. A., & Cheung, K. F. (2003). Settling Characteristics of Calcareous Sand. *Journal of Hydraulic Engineering*, *129*(6), 479–483. https://doi.org/10.1061/(ASCE)0733-9429(2003)129:6(479)

Smith, D. A., & Cheung, K. F. (2004). Initiation of Motion of Calcareous Sand. *Journal of Hydraulic Engineering*, *130*(5), 467–472. https://doi.org/10.1061/(ASCE)0733-9429(2004)130:5(467)

Southard, J. (Ed.). (2006). *Course Number 12.090: Introduction to Fluid Motions, Sediment Transport, and Current-Generated Sedimentary Structures*. Massachusetts Institute of Technology; OpenCourseWare. https://ocw.mit.edu/courses/12-090-introduction-to-fluid-motions-sediment-transport-and-current-generated-sedimentary-structures-fall-2006/

Stokes, G. G. (1850). On the Effect of the Internal Friction of Fluids on the Motion of Pendulums. *Transactions of the Cambridge Philosophical Society*, *IX*(II). https://ia600305.us.archive.org/20/items/b22464074/b22464074.pdf

Stringham, G. E., Simons, D. B., & Guy, H. P. (1969). *The behavior of large particles falling in quiescent liquids* (Professional Paper No. 562C). United States Geological Survey; USGS Publications Warehouse. https://doi.org/10.3133/pp562C

Vaz, M. F., & Fortes, M. A. (1988). Grain size distribution: The lognormal and the gamma distribution functions. *Scripta Metallurgica*, *22*(1), 35–40. https://doi.org/10.1016/S0036-9748(88)80302-8

Wadell, H. (1934). Some New Sedimentation Formulas. *Physics*, *5*(10), 281–291. https://doi.org/10.1063/1.1745211

Wang, C., Zheng, S., Wang, P., & Hou, J. (2015). Interactions between vegetation, water flow and sediment transport: A review. *Journal of Hydrodynamics*, *27*(1), 24–37. https://doi.org/10.1016/S1001-6058(15)60453-X

Wang, Y., Zhou, L., Wu, Y., & Yang, Q. (2018). New simple correlation formula for the drag coefficient of calcareous sand particles of highly irregular shape. *Powder Technology*, *326*, 379–392. https://doi.org/10.1016/j.powtec.2017.12.004

Weill, P., Mouazé, D., Tessier, B., & Brun-Cottan, J.-C. (2010). Hydrodynamic behaviour of coarse bioclastic sand from shelly cheniers. *Earth Surface Processes and Landforms*, *35*(14), 1642–1654. https://doi.org/10.1002/esp.2004

Wilde, R. H. (1952). *Effects of shape on the fall-velocity of gravel-sized particles* [Master thesis, Colorado Agricultural and Mechanical College]. https://hdl.handle.net/10217/195976

Williams, G. P. (1966). Particle roundness and surface texture effects on fall velocity. *Journal of Sedimentary Research*, *36*(1), 255–259. https://doi.org/10.1306/74D71479-2B21-11D7-8648000102C1865D

Wu, W., & Wang, S. S. Y. (2006). Formulas for Sediment Porosity and Settling Velocity. *Journal of Hydraulic Engineering*, *132*(8), 858–862. https://doi.org/10.1061/(ASCE)0733-9429(2006)132:8(858)

Yang, H.-W., Lourenço, S. D. N., & Baudet, B. A. (2022). 3D fractal analysis of multi-scale morphology of sand particles with µCT and interferometer. *Géotechnique*, *72*(1), 20–33. https://doi.org/10.1680/jgeot.19.P.120

Yim, W. W.-S. (1994). Offshore Quaternary sediments and their engineering significance in Hong Kong. *Engineering Geology*, *37*(1), 31–50. https://doi.org/10.1016/0013-7952(94)90080-9

Zhang, Z., Lan, X., Wen, G., Long, Q., & Yang, X. (2021). An Experimental Study on the Particle Size and Shape Distribution of Coal Drill Cuttings by Dynamic Image Analysis. *Geofluids*, *2021*, 1–11. https://doi.org/10.1155/2021/5588248

Zhiyao, S., Tingting, W., Fumin, X., & Ruijie, L. (2008). A simple formula for predicting settling velocity of sediment particles. *Water Science and Engineering*, *1*(1), 37–43. https://doi.org/10.1016/S1674-2370(15)30017-X

Zingg, T. (1935). Beitrag zur Schotteranalyse : die Schotteranalyse und ihre Anwendung auf die Glattalschotter. *Schweizerische Mineralogische Und Petrographische Mitteilungen*, *15*(1), 39–140. https://doi.org/10.5169/seals-15330